FUEL CELL ENTRY WALL RESPONSE TO HYDRAULIC RAM

Bruce Dean Page

NAVAL POSTGRADUATE SCHOOL
Monterey, California

THESIS

FUEL CELL ENTRY WALL RESPONSE

TO HYDRAULIC RAM

by

Bruce Dean Page

March 1975

Thesis Advisor: H. L. Power, Jr.

SECURITY CLASSIFICATION OF THIS PAGE (When Data Entered)

REPORT DOCUMENTATION PAGE		READ INSTRUCTIONS BEFORE COMPLETING FORM
1. REPORT NUMBER	2. GOVT ACCESSION NO.	3. RECIPIENT'S CATALOG NUMBER
4. TITLE (and Subtitle) Fuel Cell Entry Wall Response to Hydraulic Ram		5. TYPE OF REPORT & PERIOD COVERED Master's Thesis March 1975 6. PERFORMING ORG. REPORT NUMBER
7. AUTHOR(s) Bruce Dean Page		8. CONTRACT OR GRANT NUMBER(s)
9. PERFORMING ORGANIZATION NAME AND ADDRESS Naval Postgraduate School Monterey, California 93940		10. PROGRAM ELEMENT, PROJECT, TASK AREA & WORK UNIT NUMBERS
11. CONTROLLING OFFICE NAME AND ADDRESS Naval Postgraduate School Monterey, California 93940		12. REPORT DATE March 1975 13. NUMBER OF PAGES
14. MONITORING AGENCY NAME & ADDRESS(if different from Controlling Office)		15. SECURITY CLASS. (of this report) 15a. DECLASSIFICATION/DOWNGRADING SCHEDULE

16. DISTRIBUTION STATEMENT (of this Report)

Approved for public release; distribution unlimited.

17. DISTRIBUTION STATEMENT (of the abstract entered in Block 20, if different from Report)

18. SUPPLEMENTARY NOTES

19. KEY WORDS (Continue on reverse side if necessary and identify by block number)

20. ABSTRACT (Continue on reverse side if necessary and identify by block number)

Hydraulic ram concerns the dynamic loads and catastrophic failure of liquid-filled fuel tanks impacted by high speed projectiles. Hydraulic ram is divided into two phases: the shock phase and the drag phase. Analytical models have been proposed for the shock phase pressures by Yurkovich and for the drag phase pressures by Lundstrom. Comparisons were made between hydraulic ram fuel cell entry wall strains predicted

DD FORM 1 JAN 73 1473 EDITION OF 1 NOV 65 IS OBSOLETE
S/N 0102-014-6601 |
(Page 1)

SECURITY CLASSIFICATION OF THIS PAGE (When Data Entered)

using several loading models and those determined experimentally. A reasonable correlation was achieved but more work must be done to permit predictions of hydraulic ram strains accurate enough for the purpose of fuel cell design.

Fuel Cell Entry Wall Response to Hydraulic Ram

by

Bruce Dean Page
Lieutenant Commander, United States Navy
B.S., Iowa State University, 1964

Submitted in partial fulfillment of the
requirements for the degree of

MASTER OF SCIENCE IN AERONAUTICAL ENGINEERING

from the

NAVAL POSTGRADUATE SCHOOL
March 1975

ABSTRACT

Hydraulic ram concerns the dynamic loads and catastrophic failure of liquid-filled fuel tanks impacted by high speed projectiles. Hydraulic ram is divided into two phases: the shock phase and the drag phase. Analytical models have been proposed for the shock phase pressures by Yurkovich and for the drag phase presssures by Lundstrom. Comparisons were made between hydraulic ram fuel cell entry wall strains predicted using several loading models and those determined experimentally. A reasonable correlation was achieved but more work must be done to permit predictions of hydraulic ram strains accurate enough for the purpose of fuel cell design.

TABLE OF CONTENTS

LIST OF FIGURES

SYMBOLS

c	Speed of sound in the fluid
E	Young's Modulus
E_o	Impact Energy
h	Plate thickness
I	Current
K	Gage factor
p_i	Incident pressure
p_w	Pressure at the wall
R_2	Fixed resistance
R_g	Active strain gage
v_i	Incident fluid velocity
$\dot{w}$	Wall velocity
ε_θ	Circumferential strain
ε_r	Radial strain
η	Constant current circuit efficiency
ν	Poisson's ratio
ρ	Fluid density
σ_θ	Circumferential stress
σ_r	Radial stress

I. INTRODUCTION

Survivability of aircraft flying in a hostile arena has become increasingly important. Recent experiences have demonstrated the vulnerability of sophisticated and expensive aircraft to both small arms ground fire and the more complex surface-to-air defenses. These considerations have made necessary survivability analysis during the preliminary design phase of the aircraft procurement cycle. As a result, engineering estimates of fuel cell structural response induced when a ballistic threat penetrates a fuel tank are required.

Tactical aircraft fuel tanks or cells have the largest surface area and volume of all vulnerable components. The pressure loading associated with ballistic impact of a projectile into an aircraft fuel cell can cause aircraft loss, due to fuel starvation, explosion or fire, because fuel pressure loadings induced can damage critical components in the cell or immediately adjacent to the cell's exterior. In order to prevent or reduce damage of this nature the failure mechanisms of fuel cells must be understood. Projectiles which penetrate fluid-filled cells cause damage many times more severe than that incurred by impact with an empty cell. The interaction of the fluid-filled cell with a projectile is called hydraulic ram. This phenomenon consists of several separate and distinct components. Two phases, the shock and drag phases, are considered in this report.

The shock phase is initiated when the projectile impacts the fluid. As energy is transferred to the fluid, a strong hemispherical shock wave centered at the point of impact is formed. This creates an impulsive load on the inside of the entry wall which may cause the wall to fail.

As the projectile travels through the fluid, its energy is transformed into kinetic energy of fluid motion. A pressure field is generated as fluid is displaced from the projectile path and a cylindrical cavity is formed. Form drag decelerates the projectile, hence this phase is termed the "drag phase." In contrast to the pressures developed in the shock phase, the fluid is accelerated gradually rather than impulsively so that the peak pressure is much lower; however, the duration of the pressure pulse is considerably longer.

The cavity formed behind the projectile as it passes through the fluid is filled with liquid vapor evaporated from the cavity surface and air which can enter the cavity through the entry hole. As the fluid seeks to regain its undisturbed condition, the cavity will oscillate. The concomitant pressures will pump fluid from the cell and may be sufficient to damage fuel cell components. This oscillation is called "cavity phase."

Significant damage may also be caused during an "eruption phase." If fluid depth above the projectile trajectory is sufficiently shallow, the moving fluid during cavity formation will break through the surface and will impact the cell

top. Boeing (Ref. 1) has shown that erupting fluid can warp 3/8-inch steel plate when placed three inches above the fluid during a .50 caliber impact.

Research at the Naval Postgraduate School has been designed to isolate and observe the individual aspects of hydraulic ram. The ballistic range has been used to study energy loss due to projectile penetration of aluminum entry walls, shock propagation and drag phase pressures. This study has investigated the dynamic response of the entry wall. Comparison between responses measured on the ballistic range and those theoretically predicted were made.

II. BACKGROUND

Hydraulic ram is a phenomenon that may cause catastrophic failure of aircraft fuel cells when they are subjected to ballistic impact. The response of the fuel cell will depend on its construction. The fuel cell walls in typical combat aircraft wings are constructed of high-strength metal designed to withstand normal flight loads. Entry wall damage due to projectile penetration is usually small if the tank contains no fuel. However, damage caused by hydraulic ram to fluid-filled tanks is not so well understood and is considerably more significant. Hydraulic ram pressure loadings on the walls will cause wall motion and can result in tearing which allows fuel loss and may damage other critical aircraft components in or near the cell.

Analytical methods developed to date have considered both the shock, drag and cavity phase effects. The first effect to be considered is the shock wave that is formed when the projectile pierces the tank and impacts the fluid. As this hemispherical shock wave moves radially from the point of impact, a transient pressure pulse is created which acts on the entrance wall of the cell.

During the subsequent motion of the projectile through the fluid, a large transient cavity is formed behind the projectile. As a result, another pressure pulse is created which is felt throughout the cell. As the cavity collapses,

another cavity pressure pulse is generated which may also cause extensive damage.

Yurkovich (Ref. 2) developed an analytical method of predicting shock and cavity pressures as a function of time. Prior to this development, theories existed which described the shock front properties, but there was no analytical method available to predict the distribution of pressure throughout the tank. This prediction assumed rigid tank walls. There is very little experimental data with which to correlate these predictions. The main parameters that influence the strength of the shock phase shock wave are the energy transferred to the fluid and the fluid equation of state. The one-dimensional unsteady motion of the shock is governed by the basic conservation equations of mass, energy and momentum. The Rankine-Hugoniot equations determine the conditions at the shock front. When the input energy, undisturbed fluid density and speed of sound in the fluid are known, the pressure profile as a function of time can be computed.

After the initial impact phase, the projectile is subject to drag forces while it penetrates the bulk of the fluid. Cavitation takes place and the cavity size will vary as the projectile drag varies with time and position. Until recently, mathematical models did not allow for the closing or the changing shape of the cavity. In order to approximate the cavity, Yurkovich proposed a model which consists of several stationary, radially expanding, spherical bubbles. Incompressible potential flow theory was then applied and the assumption

was made that shock and cavity phase effects were unrelated.

A more recent analysis by Lundstrom (Ref. 3) has led to the development of a computer program which predicts fuel cell pressures at points internal to the tank during the drag phase. Lundstrom's model assumes that the projectile will tumble as it traverses the tank. The assumption was made that the flow field can be described in terms of a potential function which satisfies the wave equation. Because this problem is exceptionally difficult to solve even after making simplifying assumptions, the effects of the bullet were approximated by the action of a line of sources along the bullet path. The potential due to these sources was expressed as an integral function of the source strength, its location and the distance to the point at which the pressure was calculated. In order to account for the effects of the wall reflections, the walls were considered to be free surfaces so that reflected pressures would result from a mirror image of the line of sources creating the incident pressure. These predictions are not applicable to the wall response problem because the free surface assumption results in a boundary condition of zero pressure pertubation at the wall. Lundstrom's analysis, however, may be used in certain circumstances for the wall response problem if the image system for the wall to be studied is removed.

The wall response problem of a fluid-filled tank subjected to impact by a high speed projectile is extremely complex

because the structural and fluid equations of motion are coupled by the presence of a common interface. If these effects are to be taken into account in an exact fashion, the structure and fluid differential equations of motion must be solved simultaneously which becomes very complicated.

Ball's recent application of piston theory (Ref. 4) provides an estimate of the fluid and structure interaction during hydraulic ram. This theory provides the correct solution to the one-dimensional propagation of stresses in an acoustic medium due to a moving boundary. In general, the equations for fluid pressures and motion are coupled to those for the wall strain and motion. Application of piston theory allows the structure and fluid equations to be uncoupled. Wall response can be computed using conventional structural response equations when the incident fluid pressure p_i and velocity v_i at the wall are known. According to piston theory, the wall pressure loading p_w is given by:

$$p_w = p_i + \rho c(v_i - \dot{w}) \qquad \text{(II-1)}$$

where p_i and v_i are the incident pressure and velocity of the fluid if the wall were not there, ρ is the fluid density, c is the acoustic velocity of the fluid and $\dot{w}$ is the wall velocity. This wall pressure has terms which are independent of the wall response. These terms may be calculated, therefore, before the wall motion is known. Lundstrom's digital computer code may be used to predict the fluid pressures p_i and velocities v_i throughout the body of fluid due to the

projectile penetration and specifically to predict p_i and v_i at the entry wall as a function of time. The pressure term $\rho c\dot{w}$ was incorporated into the original structural equations of motion and the response may be calculated.

The computer program SATANS developed by Ball (Ref. 5) has been used to calculate the wall response due to the hydraulic ram time varying pressure distribution. It predicts the geometrically non-linear response of arbitrarily loaded shells of revolution. The program can be used to analyze any shell of revolution for which the following conditions hold:

1. The geometric and material properties of the shell are axisymmetric.
2. The applied pressure and temperature distributions and initial conditions are symmetric about a datum meridional plane.
3. The shell material is isotropic and the Poisson ratio is constant.
4. The boundaries of the shell may be closed, free, fixed or elastically restrained.

A fuel cell entry wall is a simple axisymmetric shell with zero curvature. The governing partial differential equations are based upon Sander's non-linear thin shell theory. The equations are reduced to uncoupled sets of four linear, second order, partial differential equations in the meridional and time coordinates. The derivatives with respect to the meridional coordinate are approximated by central finite differences and the displacement accelerations are approximated by the implicit Houbolt backward difference scheme with a

constant time interval. At each time step the equations are solved until all solutions have converged.

III. THE EXPERIMENT

This experiment simulates entry wall strain present in an aircraft fuel cell as the result of the impact of a high energy projectile. Most of the analysis of hydraulic ram effects on tank walls has focused on the final or resulting damage. Little consideration has been given to determining the dynamic wall response immediately preceding failure. This experiment measures the actual time history of entry wall strain for a variety of wall thickness and impact energy level combinations so that comparison with existing analytical models can be made.

The ballistic range components used are shown in Figures III-1 and III-2. Each AVTRON, No. A914T333 chronograph screen had a five volt D.C. signal shorted to ground across it. When these screens were broken by the passage of the bullet, the interrupted circuits provided start and stop pulses to the Monsanto 101B counters and oscilloscope trigger. The counters provided time interval information which was used to determine the bullet impact velocity.

The tank used is pictured on its stand in Figure III-3. The cubical tank had inside dimensions of 17 inches. The bottom and two sides were 0.09 in. 7075-T6 aluminum welded to the $\frac{1}{4}$-inch thick by 3-inch aluminum frame. The front and back walls were bolted to the inside of the 1-inch thick aluminum front and rear wall supports which had a 15-inch

diameter circular cutout. The top was left open to simulate a fuel cell with ullage.

Three 7075-T6 aluminum entry wall test plates were used in this experiment. Each had a 1-inch diameter hole cut in the center to allow bullet entry directly into the fluid. This entry wall hole was covered with cloth tape so that the tank could be filled with water. Plates of thickness 0.05, 0.09 and 0.16 in. were tested. Four EA-13 type 175.0 OHM strain gages were located 2 inches from the center of each plate. One pair was oriented radially with one gage on the inside and one on the outside of the entry wall. The second pair of gages was oriented perpendicular to the first pair at the same radial distance from the impact point. This strain gage arrangement is pictured in Figure III-4.

Two projectile energy levels were tested for each of the three test plates. Projectile mass and velocity were used to adjust the impact energy level and this information is listed in tabular form on Figure III-5.

The recording system consisted of a dual-bean oscilloscope with two 1A7 pre-amp plug-in units with differential input capability and a Polaroid scope camera. A wiring diagram for the constant current strain gage circuits is shown in Figure III-6. Since only dynamic response was measured, temperature compensation was not required since the strain variations occurred at frequencies much higher than temperature fluctuations. The constant current method used presents practically noise free data with high sensitivity and linearity. Gage response was recorded for a pair of gages with similar orientation.

The effect of hydrostatic pressure on the wet gage output was considered. Hydrostatic pressure will cause an added strain in the filament of the wet gage which will be superimposed upon the plate surface strain. Tests on strain gages similar to those used in this experiment were conducted at the University of Illinois (Ref. 6) in order to determine the effects of high hydrostatic pressure. In testing to pressures as high as 25,000 PSI it was found that the effects of pressure on the strain gages themselves was only 2 to 5 microinches per inch of indicated compressive strain per 1000 PSI. This pressure effect was considered negligible for this study since maximum error due to this factor would amount to no more than a $\pm$50 μin/in error.

All of the ammunition was hand loaded so that the velocities could be adjusted for the desired energy level. The rifle used, a Remington .222, was fixed to an adjustable mount. It was aimed before each shot by sighting the target hole through a high power scope. This arrangement is pictured in Figure III-7. Aiming for each shot was required because the tank and rifle stands moved as the result of each shot.

Stein (Ref. 7) has shown that the constant current circuit such as used in this experiment has the ratio of output to input given by:

$$\frac{e}{\epsilon} = IR_g K \left[\frac{\eta}{1 - (1-\eta)\epsilon K}\right] \qquad \text{(III-1)}$$

where the efficiency is given by:

$$\eta = \frac{R_2}{R_2 + R_g} \qquad \text{(III-2)}$$

K is the gage factor, I the current, R_2 is the load resistance, and R_g the active gage resistance. For the circuit in these tests, equation III-1 becomes:

$$\varepsilon = \frac{e(1-0.863\varepsilon)}{2.834} \qquad \text{(III-3)}$$

Because the strains considered are several magnitudes smaller than 1, this equation can be simplified to the linear relationship:

$$\varepsilon = 0.3529e \qquad \text{(III-4)}$$

Equation III-4 was used to convert the output voltage, measured directly from photographs made of the oscilloscope trace, to surface strain.

Accompanying the distribution of forces on the entry wall is a deformation and strain. Strain is represented by the lengthening (+ for tension) or shortening (- for compression) of a straight line on the surface of the material. When a variable resistance wire strain gage is bonded to a surface, any change in length of that surface will be reflected by a change in the resistance of the gage. The concept of strain is illustrated in Figure III-8. The pure bending case as shown in Figure III-8,a is characterized by a compression of the strain gage on one surface and an equal tension in the strain gage on the opposite surface. A wall which undergoes pure stetching is characterized by equal tension

in both gages as shown in Figure III-8.b. Figure III-8.c shows a superposition of these two simple cases which results from the combined load.

The experimental strain measurements are shown in Figures III-9 through III-18. These show strain measured at two inches from the impact point in the radial and circumferential directions. The upper photograph represents radial strains with the upper most trace being the wet or fluid backed surface. The lower picture shows the circumferentail pair of gage readings with the upper trace representing the outside or dry gage. For each plate thickness at the lower energy level, various oscilloscope sweep rates were used to provide accurate information for different time intervals. Shots taken at the higher energy level resulted in considerable tank leakage and strain gage failure. As a result, less data are available. High energy shots on the 0.05 thickness plate resulted in permanent plate deformation that was not evident at the lower energy level. Significant deterioration of the strain gage bond accompanied each shot at this energy level. The strain gages could withstand no more than two shots at 12323 in-lb energy level before the bond was completely destroyed.

The traces were initiated by the breaking of a triggering screen mounted close to the front wall of the tank. The strain trace was relatively constant until bullet impact with the water. An exact impact time cannot be determined from these traces because of uncertainties in scope triggering

circuitry delay time. For purposes of this analysis, time of impact (t=0) has been taken as that time at which the first significant slope discontinuity of strain occurs.

Using Figure III-12 as typical, the results may be qualitatively interpreted as follows. In the upper picture, the first significant deflection shows the wet or inner surface gage in compression and the outer or dry gage in equal tension for approximately 60μsec. This represents almost pure bending of the wall. During the remainder of the 200μsec. interval both traces return to neutral. From that point, the lower trace continues below the neutral reading which is indicative of radial stretching. The relatively symmetrical variations in the two traces from that point on show a continuation of back and forth bending, but the displaced lower trace shows that the plate has stretched and is no longer in its original position. The lower picture in Figure III-8 shows the traces for the circumferentially oriented gages. Like the radially oriented gages, they show primarily pure bending during the first 60μsec. The strains, however, do not return to neutral but show a much more gradual stretching compared with the radial gages. The maximum strain amplitude of both radial and circumferential traces is approximately 1.4×10^{-3} in/in.

Figures III-9, 12, and 15 show the effect of plate thickness on the maximum strain amplitude. For the two larger plate thicknesses, the strains for the first 60μsec. appear to be primarily due to plate bending. The 0.05 thickness

plate, however, (Figure III-9) shows radial stretching during this time interval. The maximum radial bending strain amplitude in the 0.16 in. thick plate was found to be 0.85 x 10^{-3} in/in. The maximum bending strain in the 0.05 in. thick plate was found to be 2.2 x 10^{-3} in/in. These results show the expected increase in both bending and stretching as plate thickness is reduced.

Insufficient data exist to determine the nature of the increase in strain due to higher energy. However, a comparison of Figures III-15 and III-18 illustrates the increase in strain due to the higher hydraulic ram loading.

Figures III-11 and III-14 show the wall response for 10 milliseconds. This clearly demonstrates that significant strain is experienced by the tank entry wall well beyond the initial peak strain discussed previously.

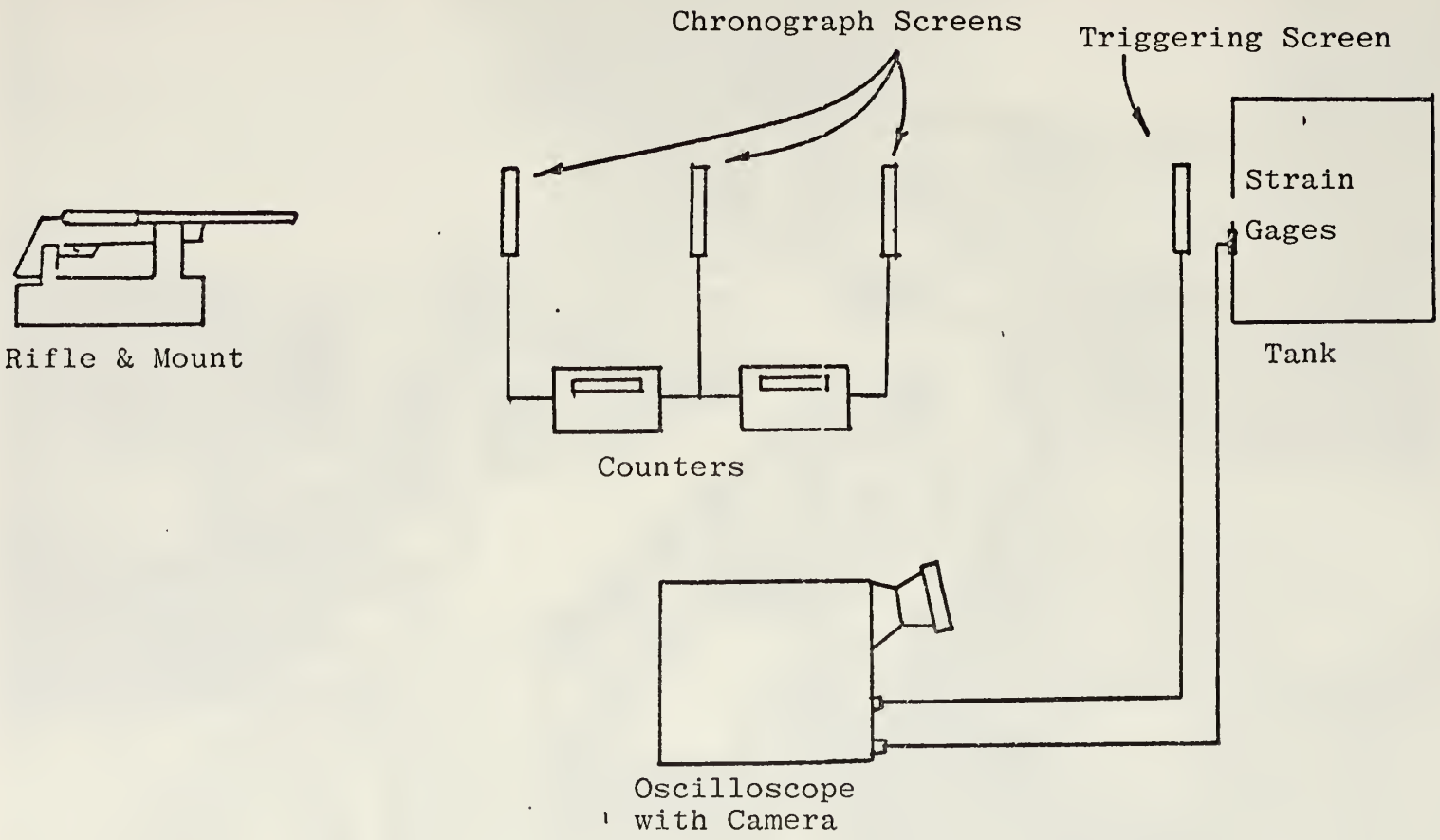

Figure III-1. Ballistic Range Components

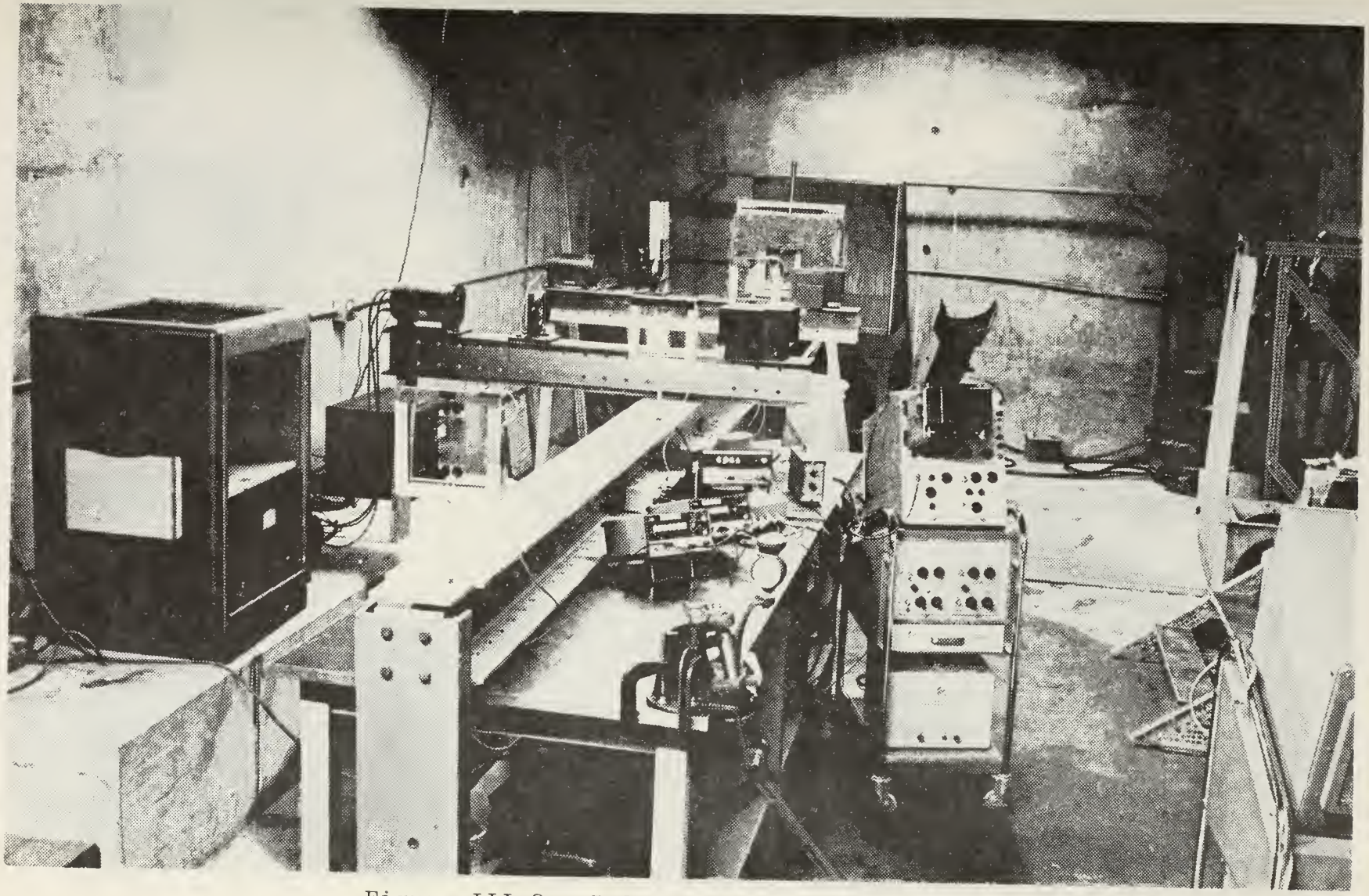

Figure III-2. Ballistic Range (Down Range View)

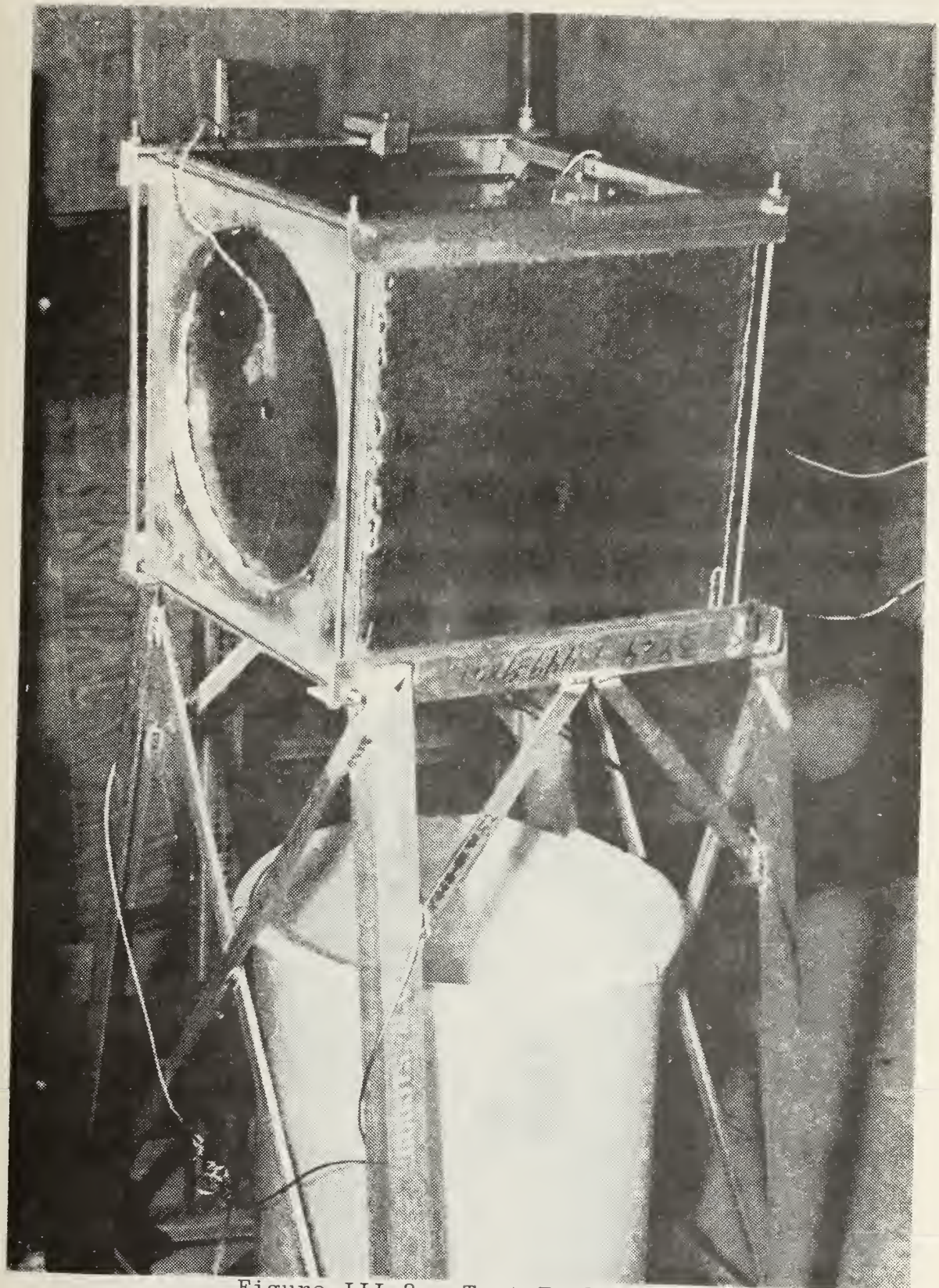

Figure III-3. Test Fuel Cell

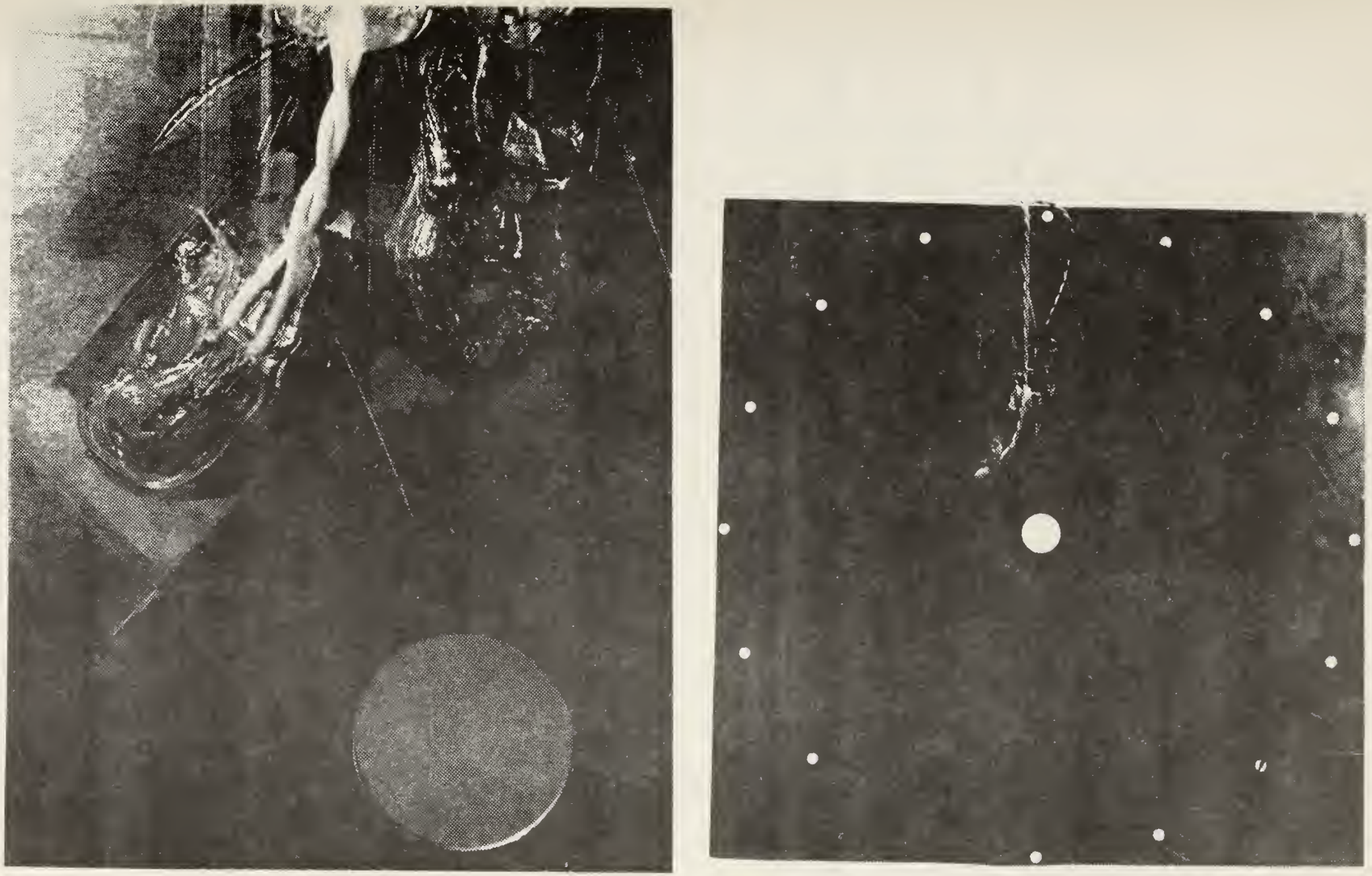

Figure III-4. Strain Gages Mounted on Entry Wall

caliber	.222 Remington	.222 Remington
Impact Velocity (ft/sec)	2500	2900
Projectile Mass (lbm)	6.43×10^{-3}	7.85×10^{-3}
Impact Energy, E_o (in-lb)	7493	12,323

Figure III-5, Projectile Parameters

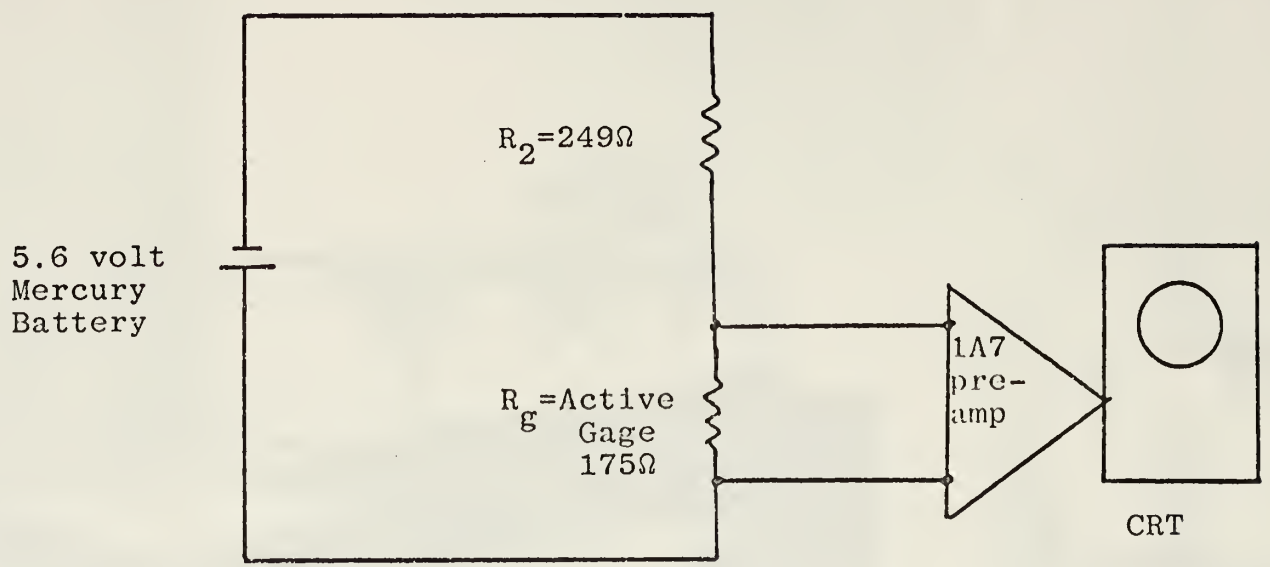

Figure III-6. Dynamic Strain Gage Circuit

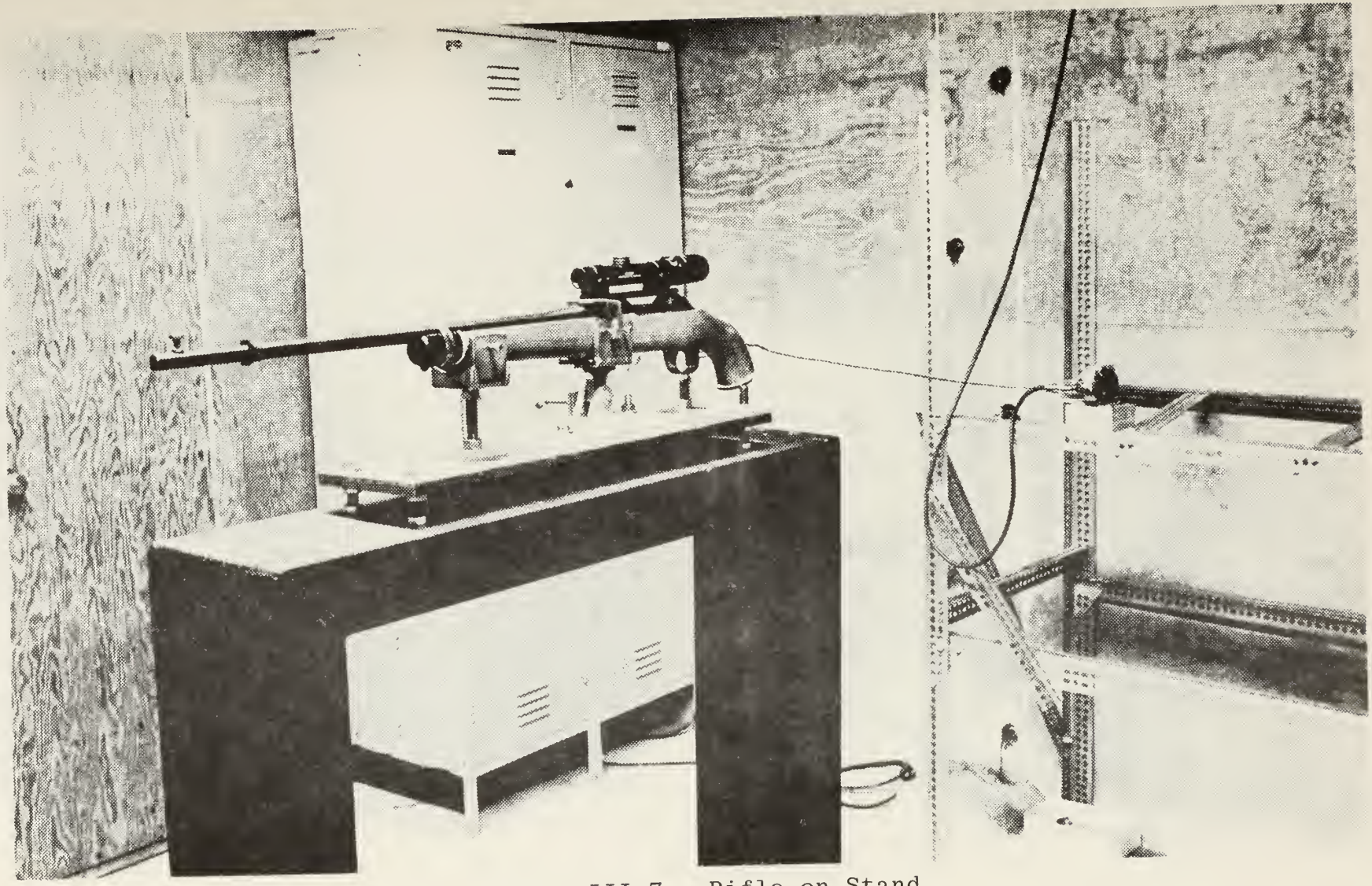

Figure III-7. Rifle on Stand

— Strain Gage

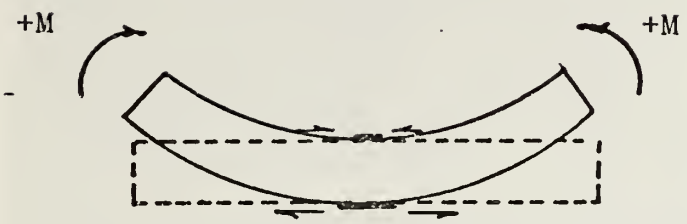

a) Strain Due to Bending

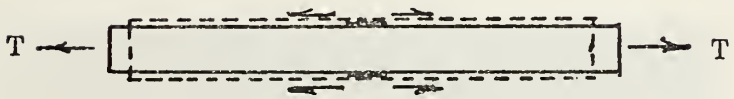

b) Strain Due to Stretching

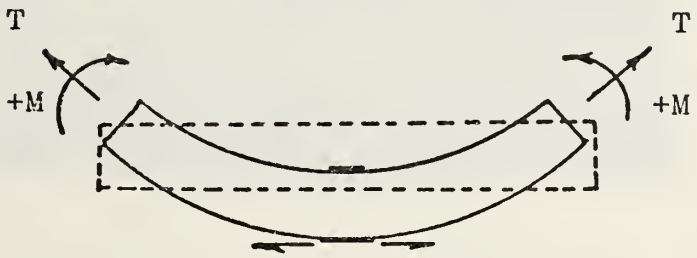

c) Strain Due to Both Bending & Stretching

Figure III-8. Strain Due to Loading

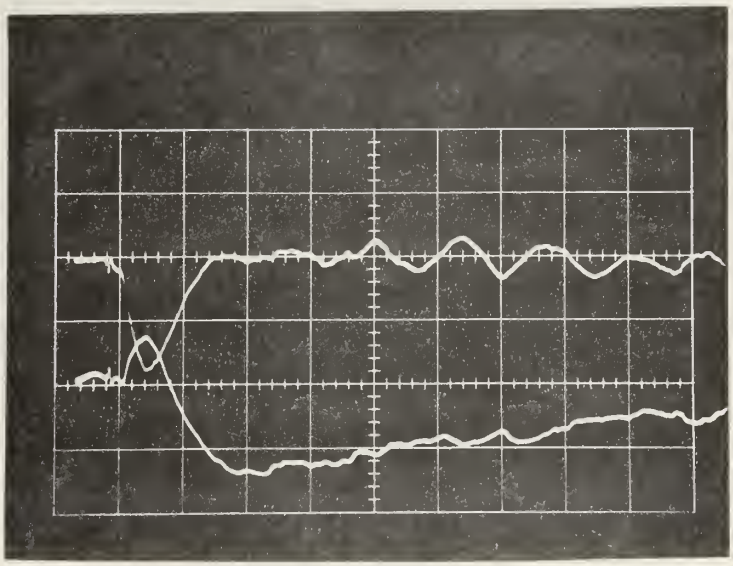

Radial Gages
200μsec/cm 5 mvolts/cm

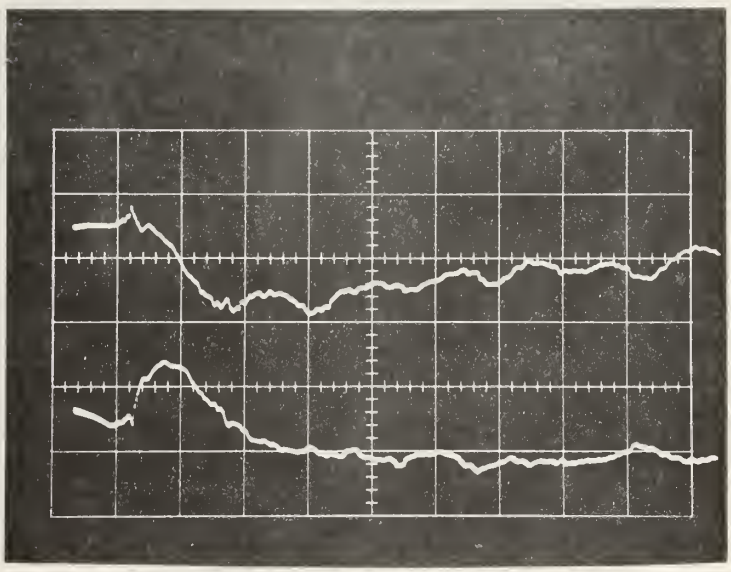

Circumferential Gages
200μsec/cm 5 mvolts/cm
h (thickness) = .05 in

Figure III-9. Entry Wall Strain (E_o = 7493 in-lb)

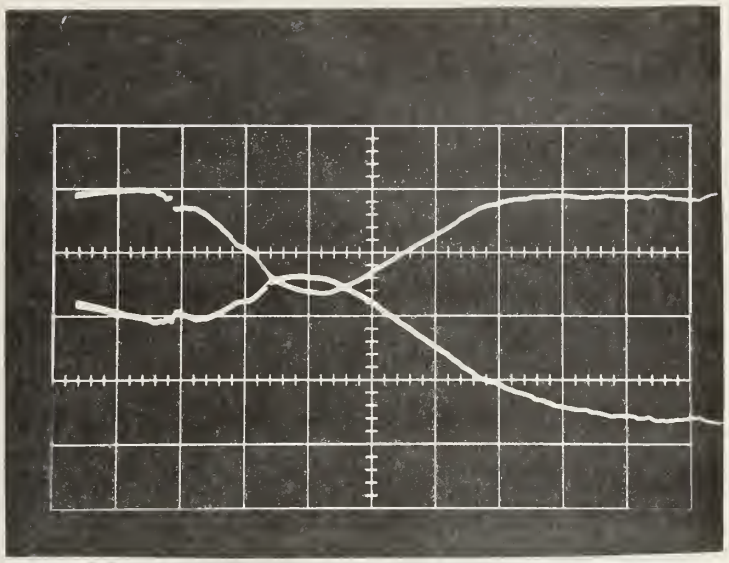

Radial Gages

50μsec/cm 5 mvolts/cm

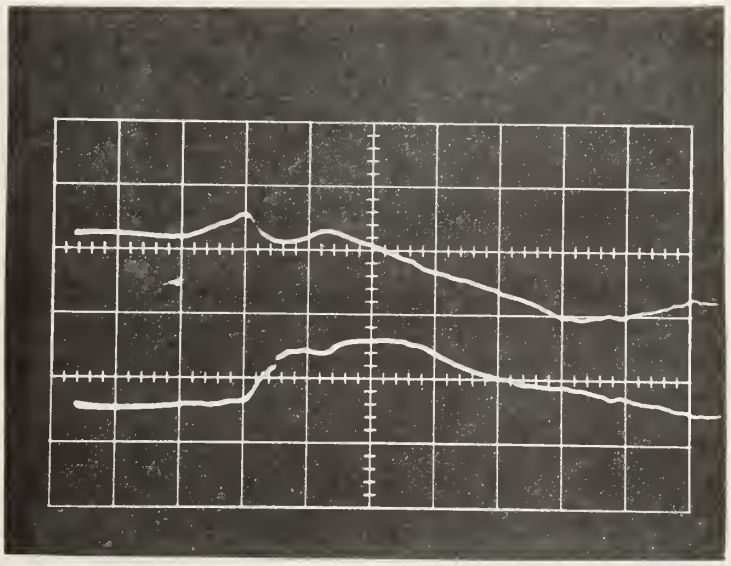

Circumferential Gages

50μsec/cm 5 mvolts/cm

h (thickness) = .05 in.

Figure III-10. Entry Wall Strain (E_o = 7493 in-lb)

Radial Gages

1 msec/cm 2 mvolts/cm

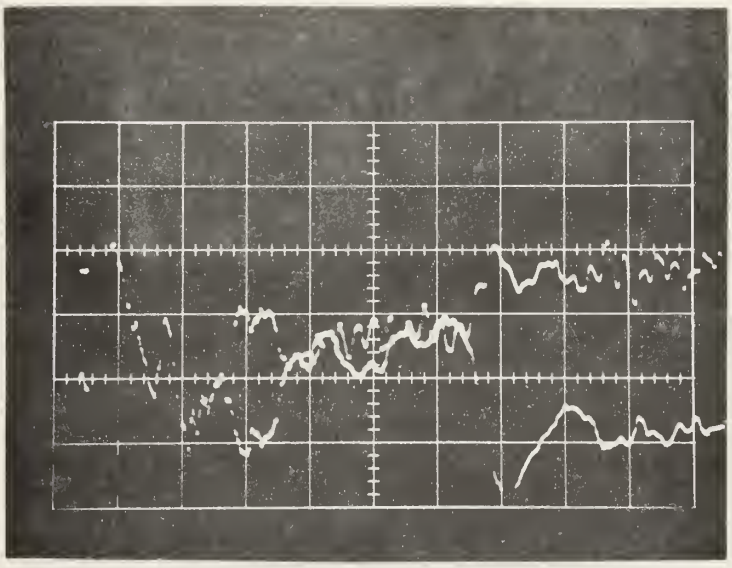

Circumferential Gages

1 msec/cm 2 mvolts/cm

h (thickness) = .09 in.

Figure III-11. Entry Wall Strain (E_o=7493 in-lb)

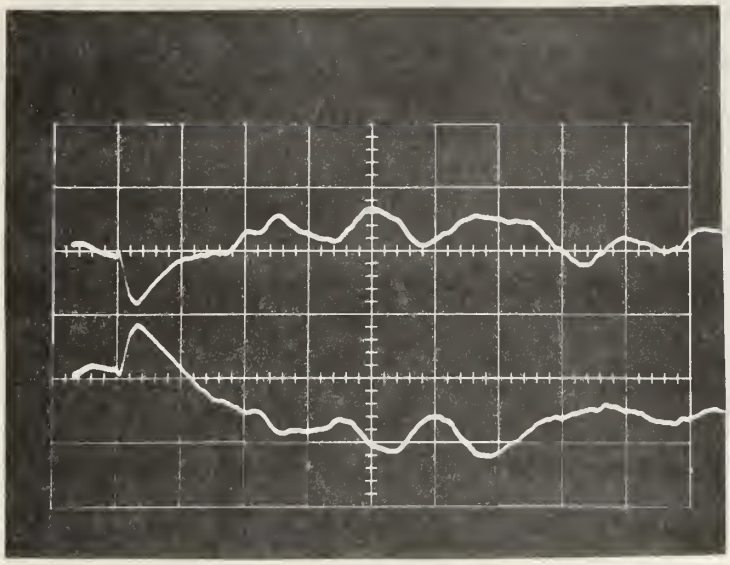

Radial Gages

200μsec/cm 5 mvolts/cm

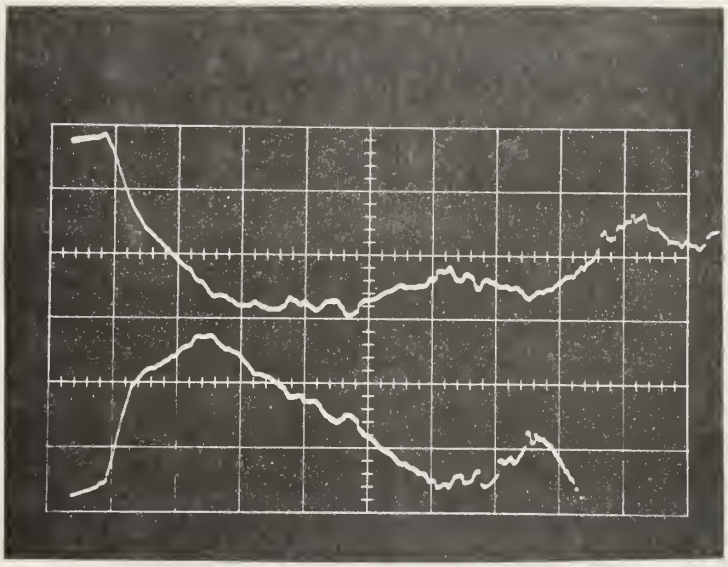

Circumferential Gages

200μsec/cm 2 mvolts/cm
h (thickness) = .09 in.

Figure III-12. Entry Wall Strain (E_o= 7493 in-lb)

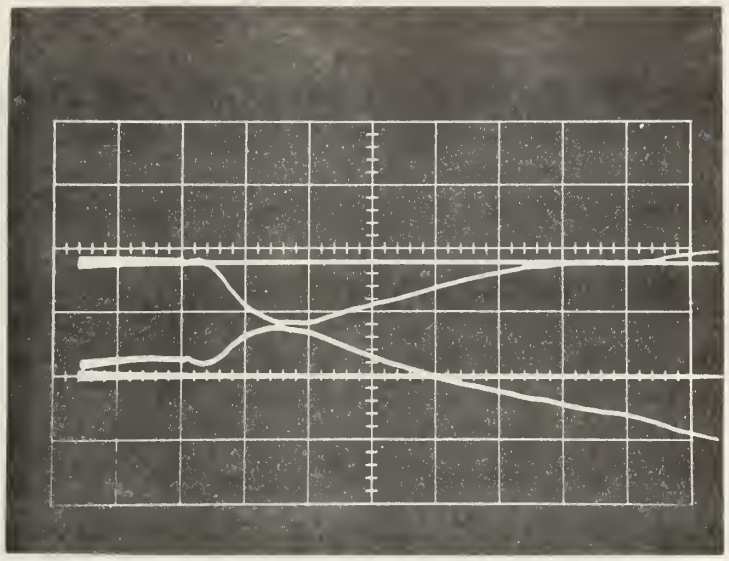

Radial Gages

50μsec/cm 5 mvolts/cm

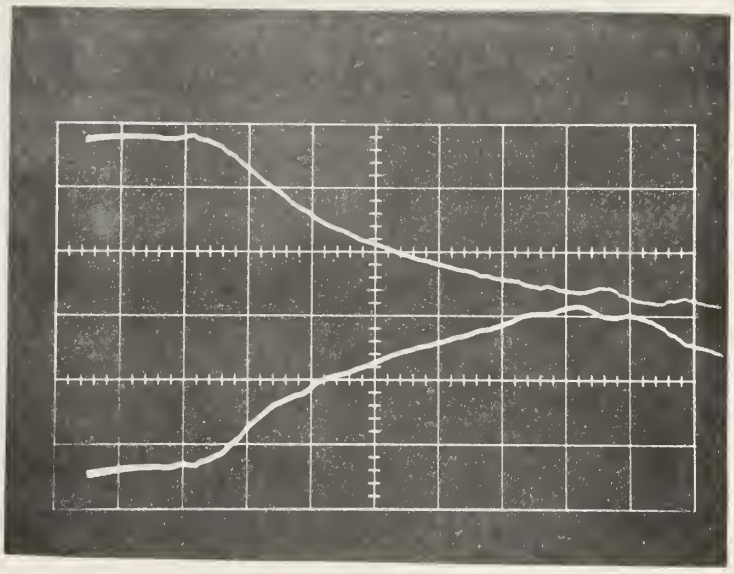

Circumferential Gages

50μsec/cm 2 mvolts/cm

h (thickness) = .09 in.

Figure III-13. Entry Wall Strain (E_o= 7493 in-lb)

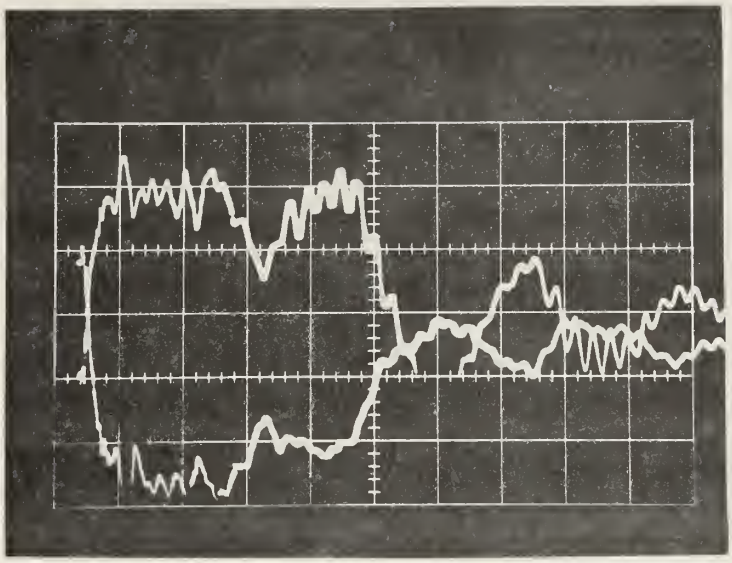

Radial Gages
1 msec/cm 2 mvolts/cm

Circumferential Gages
1 msec/cm 2 mvolts/cm

h (thickness) = .16 in.

Figure III-14. Entry Wall Strain (E_o= 7493 in-lb)

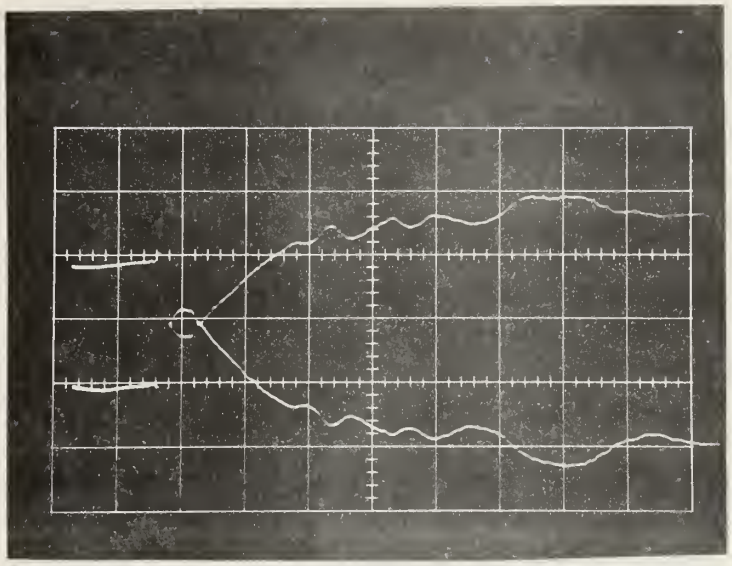

Radial Gages
100μsec/cm 2 mvolts/cm

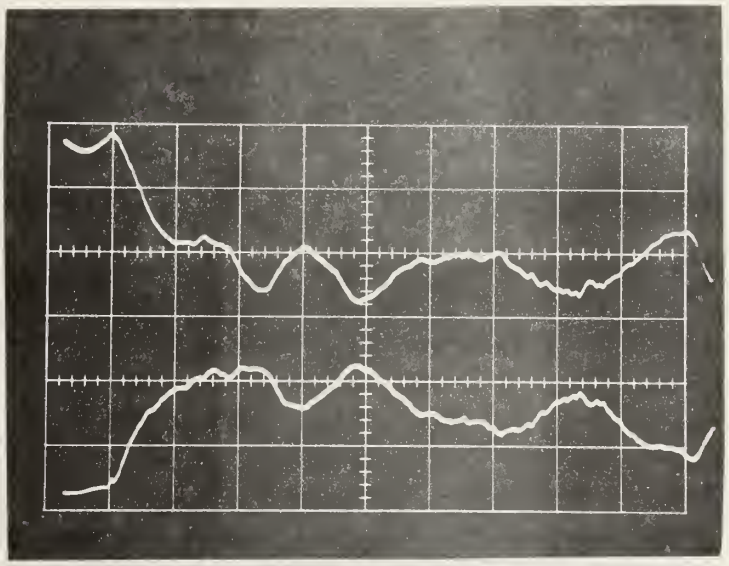

Circumferential Gages
200μsec/cm 2 mvolts/cm

h (thickness) = .16 in.

Figure III-15. Entry Wall Strain (E_o= 7493 in-lb)

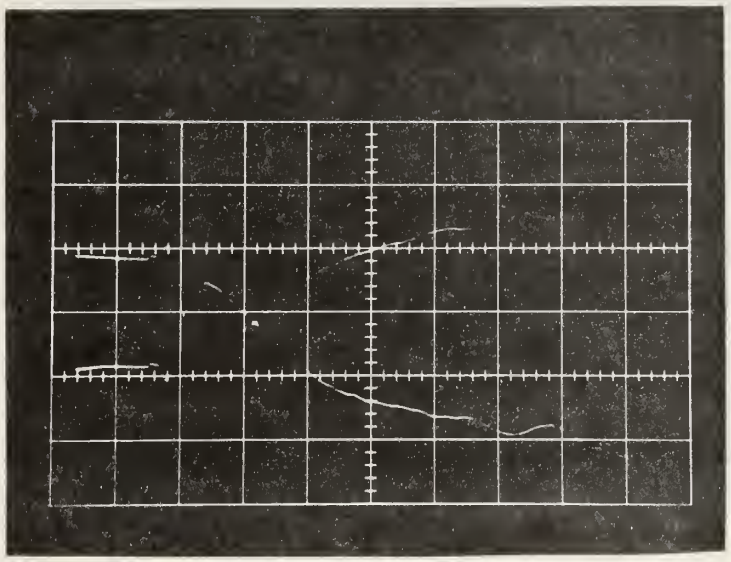

Radial Gages
50μsec/cm 2 mvolts/cm

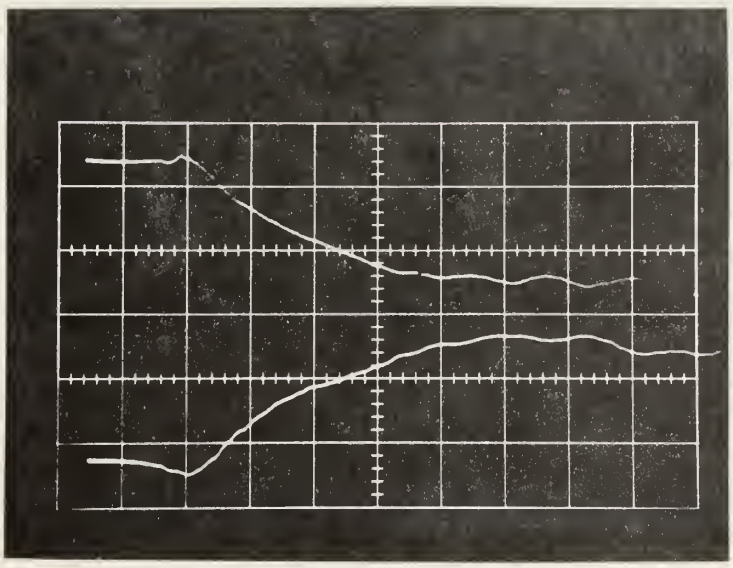

Circumferential Gages
50μsec/cm 2 mvolts/cm

h (thickness) = .16 in.

Figure III-16. Entry Wall Strain (E_o= 7493 in-lb)

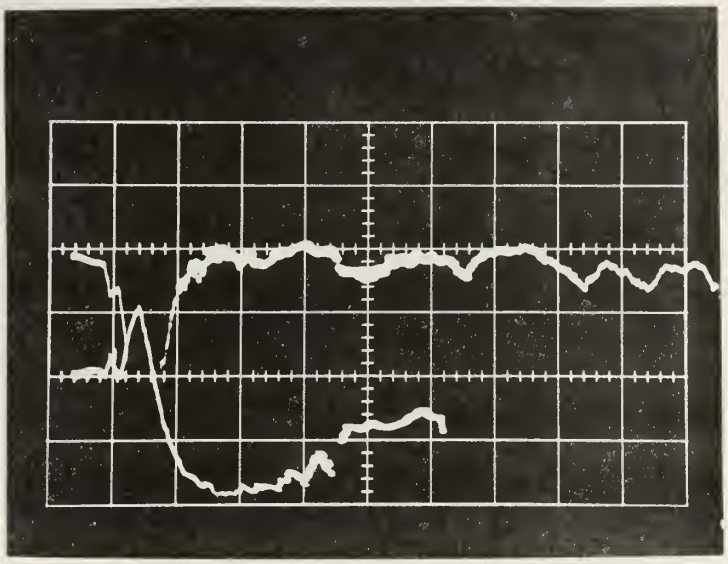

Radial Gages
200μsec/cm 5 mvolts/cm

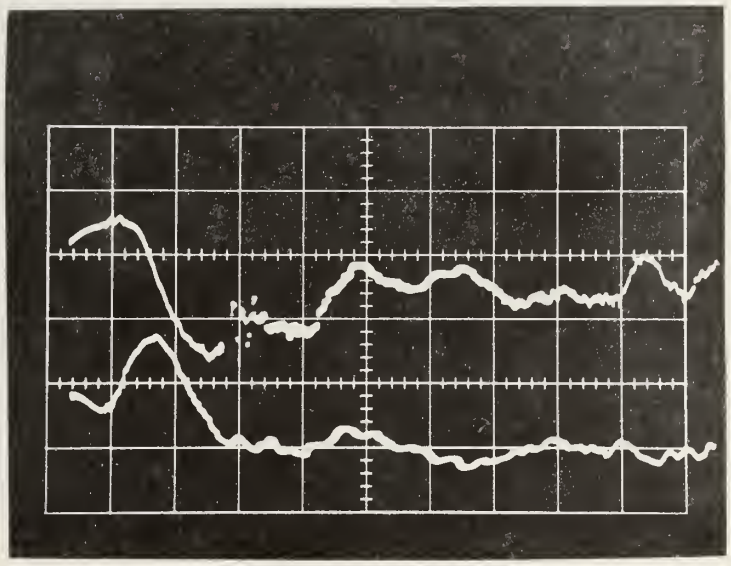

Circumferential Gages
200μsec/cm 5 mvolts/cm

h (thickness) = .05 in.

Figure III-17. Entry Wall Strain (E_o= 12,323 in-lb)

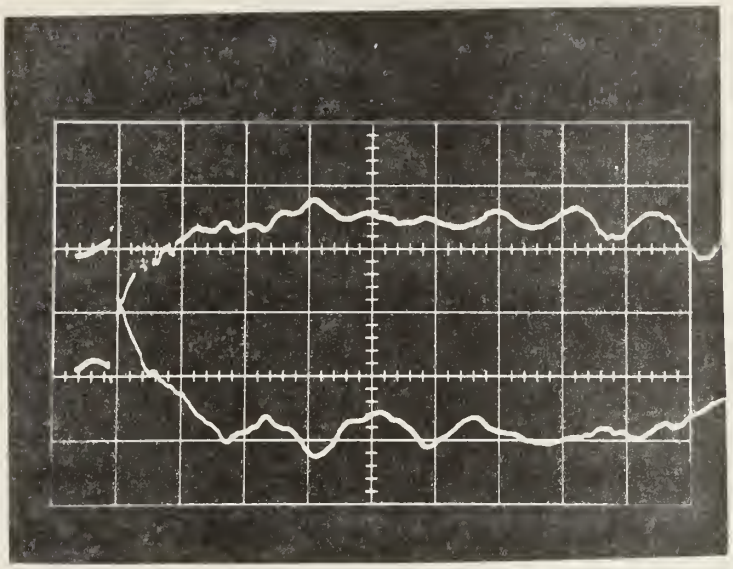

Radial Gages
200μsec/cm 5 mvolts/cm

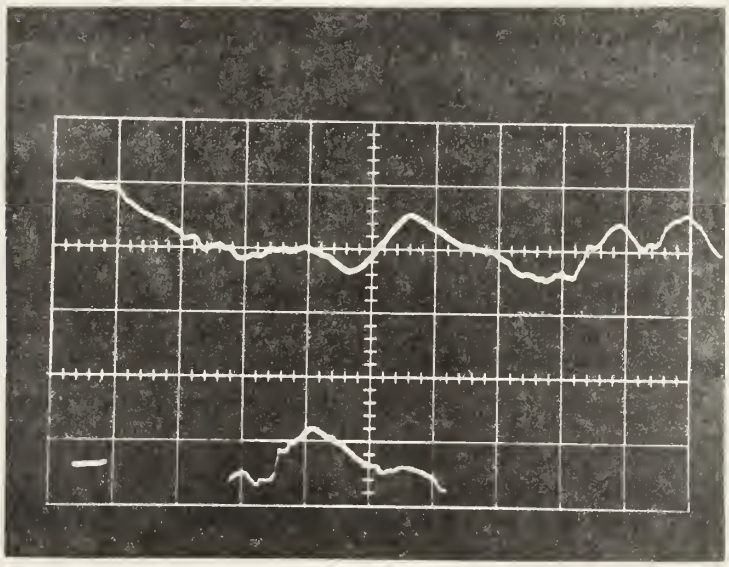

Circumferential Gages
200μsec/cm 5 mvolts/cm
h (thickness) = .16 in.

Figure III-18. Entry Wall Strain (E_o= 12,323 in-lb)

IV. ANALYSIS AND COMPARISON

An understanding of tank wall response due to hydraulic ram phenomena is necessary in order to intelligently design tank construction which reduces damage. This experiment measured entry wall strain in order to evaluate the adequacy of existing methods for predicting structural response.

For purposes of comparison, the 0.09 in. thickness plate and low energy level was selected. Predictions of strains were made using SATANS. The assumption was made that the response is axisymetric. The input parameters to SATANS were:

KMAX = 71 (number of meridional stations)

NU = 0.33 (Poisson's ratio)

DELOAD = 1×10^{-6} sec (time increment)

DEL = 0.1 (radial increment)

MASS = $\frac{0.1}{386} \times 0.09$ (plate mass per unit area)

$B = \frac{Eh}{1-\gamma^2} = 1.009 \times 10^7$ (plate in-plane stiffness)

$D = \frac{Eh^3}{12(1-\gamma^2)} = 6.8 \times 10^3$ (plate bending stiffness)

Drag phase incident pressures were calculated as a function of time for the first 500μsec, after impact using the computer program by Lundstrom (Ref. 8). This program calculates drag phase pressures accurately for times less than that required for pressure disturbances to reflect off the cavity surface. Shock phase loadings were calculated using the computer program developed at the Naval Postgraduate School (Ref. 9).

These analyses have been successful in predicting pressures internal to the tank configuration used in this experiment (Ref. 10).

Three different entry wall responses were calculated. The first case assumed no fluid-wall interaction. The wall loading was taken to be the incident pressure p_i which contained both shock and drag phase pressure predictions. Figure IV-1 and IV-2 show a comparison of this result with the experiment. It is evident that ignoring the reduction of the fluid pressure on the wall due to the wall motion results in predicted wall strains that are very large compared with those measured. This analysis predicts strains that are sufficiently large to cause permanent set. The experimental entry walls do not show any such behavior. It is clear from this result that the inclusion of the fluid-wall interaction is necessary if reasonable predictions of wall response are to be made.

The second entry wall response prediction assumed that the fluid-wall interaction could be modeled by piston theory. The wall loading was given by $p_i + \rho c v_i$ and SATANS was modified by Ball to include the $\rho c \dot{w}$ term in the structural equations of motion. The velocity v_i was taken as the normal component of the incident fluid velocity at the wall. The results from SATANS for the radial and circumferential strains ε_r and ε_θ at the strain gage location are given in Figures IV-3 and IV-4 for the $p_i + \rho c v_i$ pressure. Also shown in these figures are the corresponding experimental strains. Figures IV-5 through IV-7 show the pressure profile along the plate for $p_i + \rho c v_i$ and p_i at three different times. Note in these figures the

very high pressure in the neighborhood of the plate center for the $p_i + \rho cv$ loading. The net pressure at the plate, i.e., $p_i + \rho c(v_i - \dot{w})$, where $\dot{w}$ is obtained from the SATANS results, is also plotted in Figures IV-5 through IV-7. An examination of Figures IV-3 and IV-4 reveals that the predicted strains are considerably larger than the measured strains. A possible explanation for this behavior is the very large loading of the plate center due to ρcv_i. Figures IV-5 through IV-7 show that there is a large net pressure at the plate center due to ρcv_i that increases with time.

The third entry wall response prediction assumed that the wall loading could be approximated by $2p_i$. This pressure loading corresponds to assuming that the term ρcv_i can be replaced by p_i as in the case of a one-dimensional wave reflecting off a rigid wall. Figures IV-8 and IV-9 compare this prediction and the experimental results. Figures IV-5 through IV-7 show the net wall pressure loading calculated for this case. The replacement of the ρcv_i term by p_i results in a net wall pressure that eliminates the large loading at the center of the plate that was exhibited by the previous solution. As a result the strains predicted are much closer to those measured.

Consider the strain plots shown in Figures IV-8 and IV-9. A peak strain is evident at 35 μsec which corresponds to the arrival of the shock front at the gage location. The predicted strain then decreases dramatically, only to increase again when the effects of the drag phase pressures are felt. The experimental results do not exhibit the characteristics of the first

calculated peak. This indicates that the entry wall does not respond as predicted to the shock phase. The prediction also underestimates the wall strain due to the drag phase pressure but is quite similar in shape. Note that the predicted circumferential strains are considerably below those measured.

Stress levels at the gage for this low energy case reach approximately 21,000 psi which is well within the elastic limit of the material. This was determined from the following relationships where $E = 10^7$, $\gamma = .33$ and ε_r and ε_θ were taken from the data photographs.

$$\sigma_r = \frac{\varepsilon}{1-\gamma^2} (\varepsilon_r - \gamma\varepsilon_\theta) \qquad \text{IV-1}$$

$$\sigma_\theta = \frac{\varepsilon}{1-\gamma^2} (\varepsilon_\theta - \gamma\varepsilon_r) \qquad \text{IV-2}$$

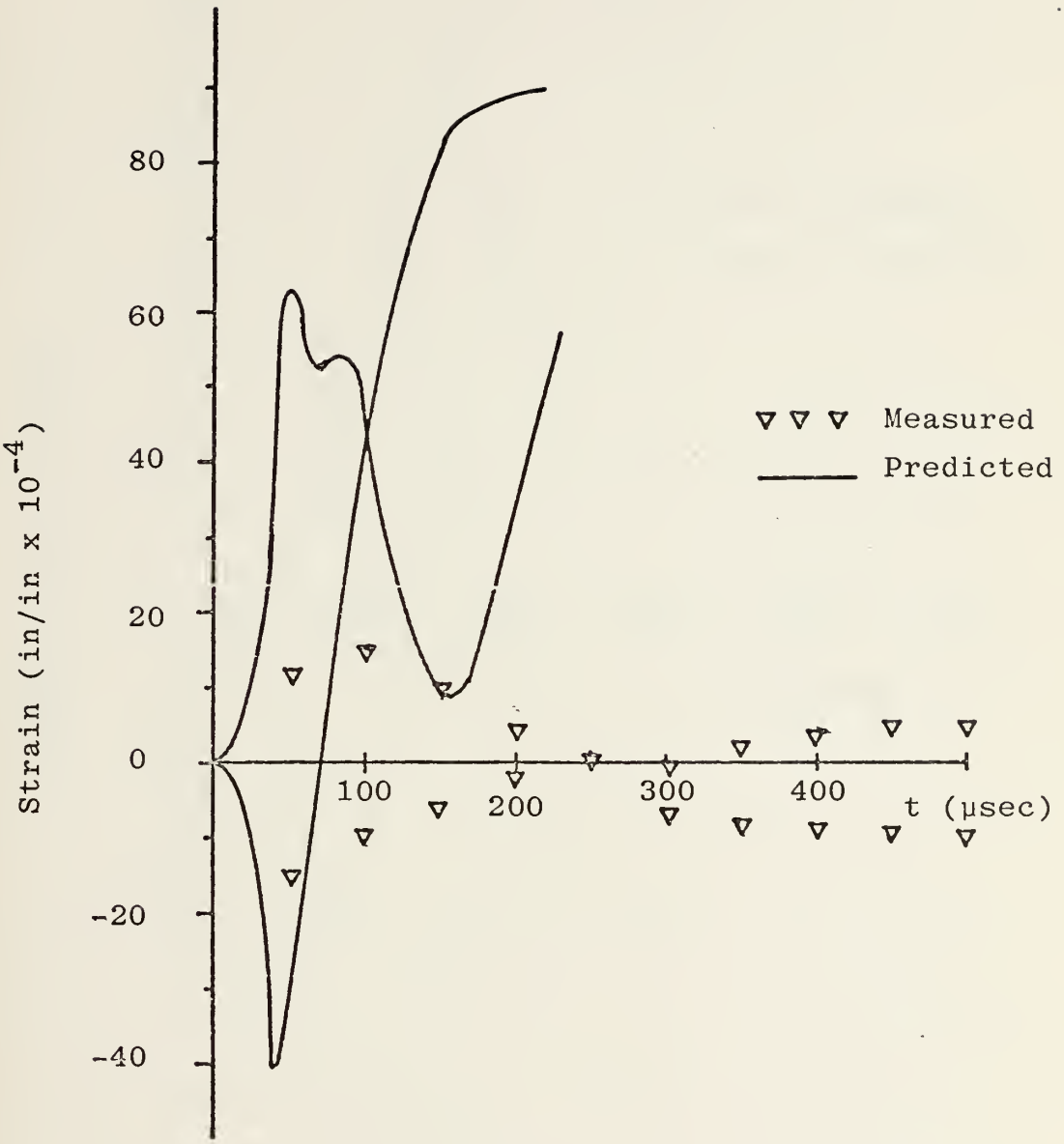

Figure IV-1. Radial Wall Strain Without Fluid-Wall Interaction

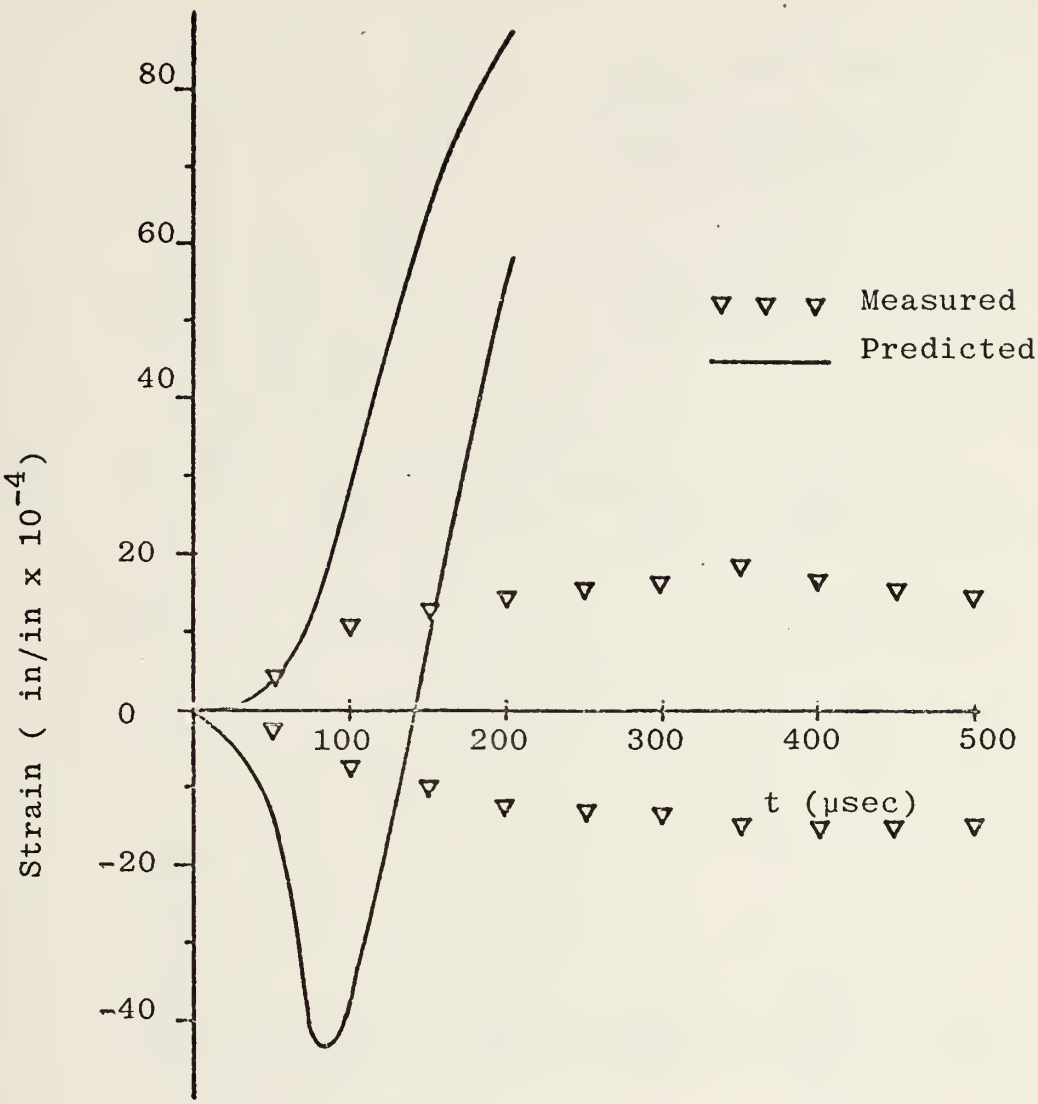

Figure IV-2. Circumferential Wall Strain Without Fluid-Wall Interaction

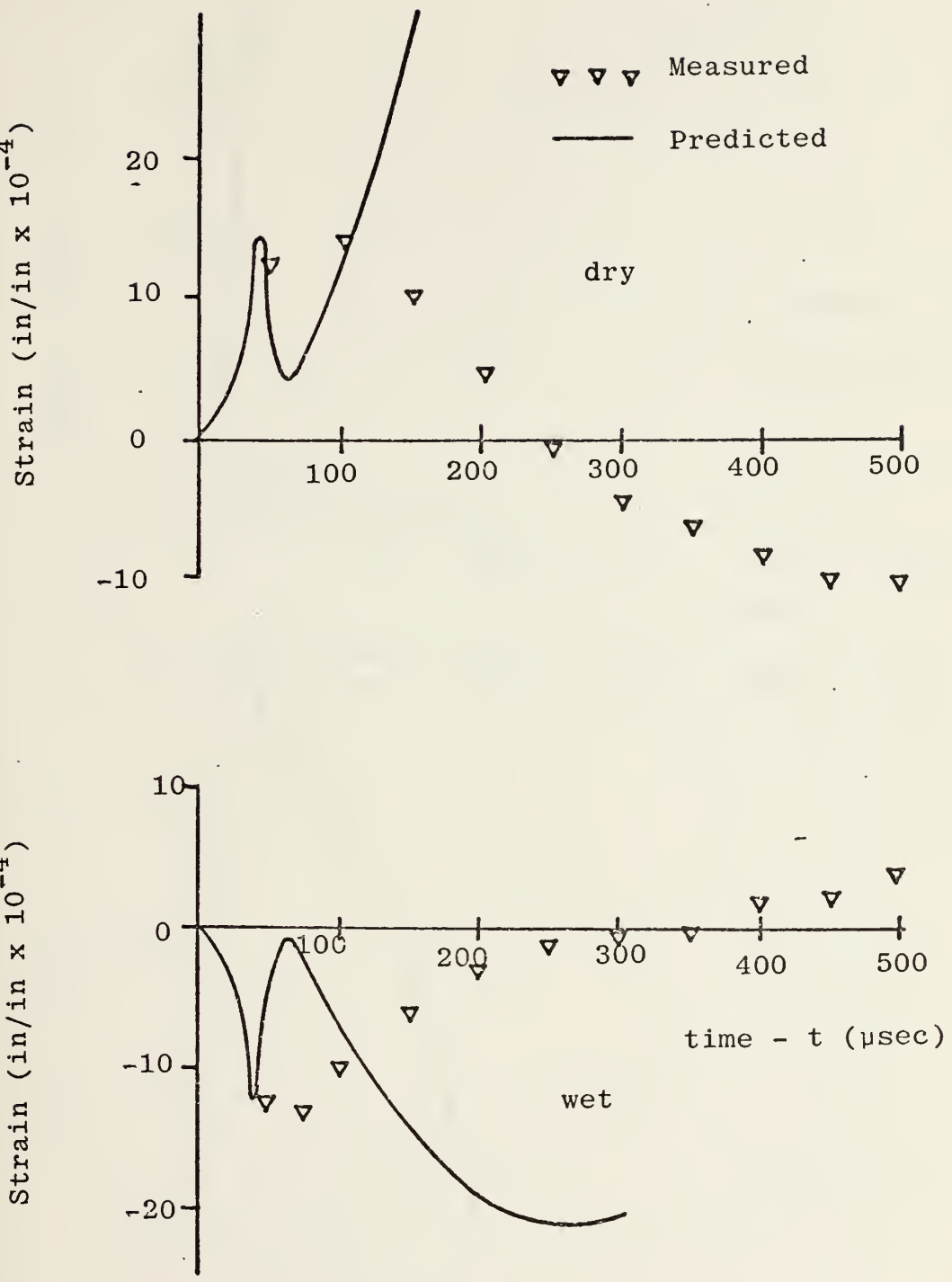

Figure IV-3. Radial Wall Strain With Piston Theory

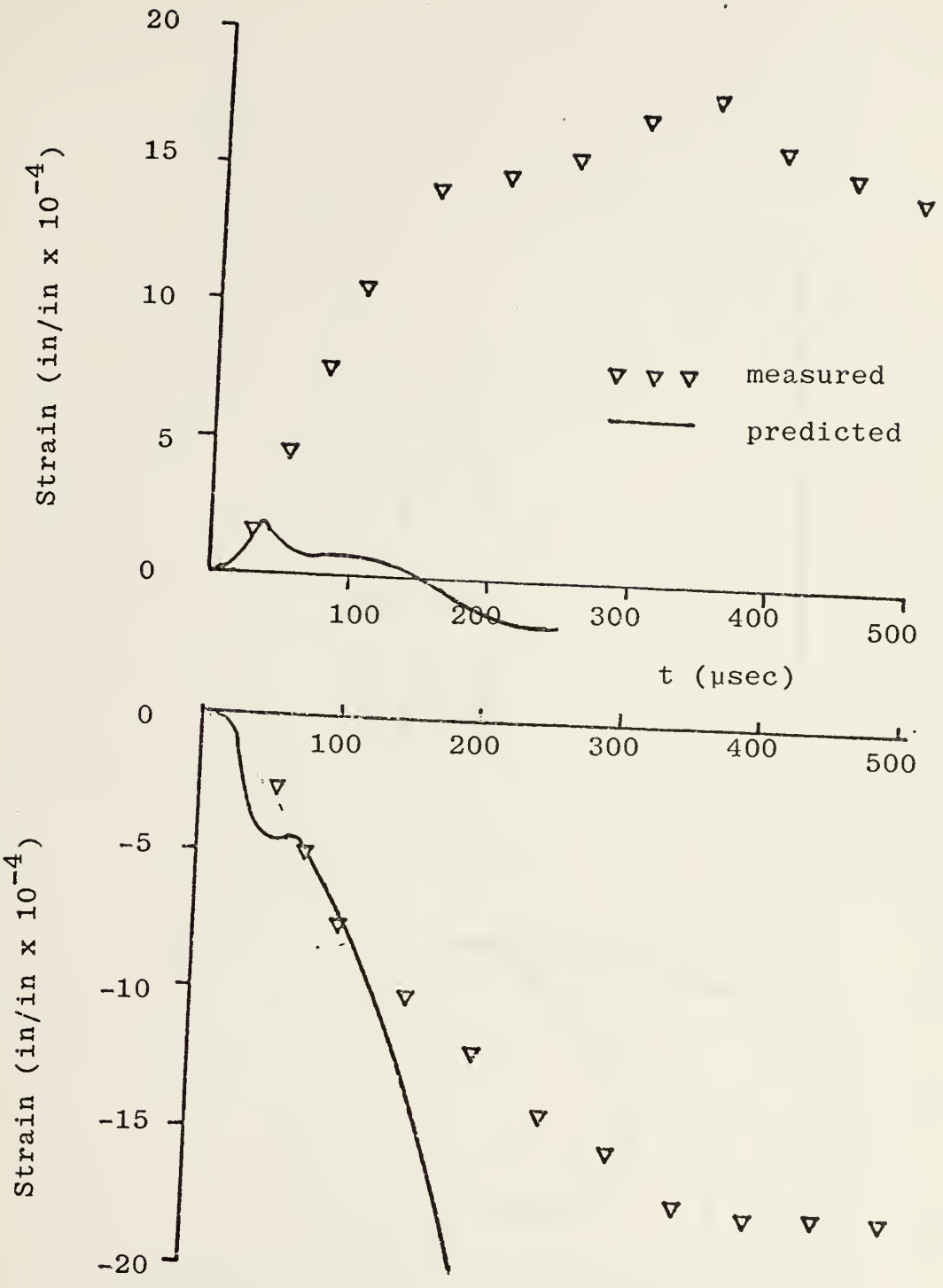

Figure IV-4. Circumferential Wall Strain With Piston Theory

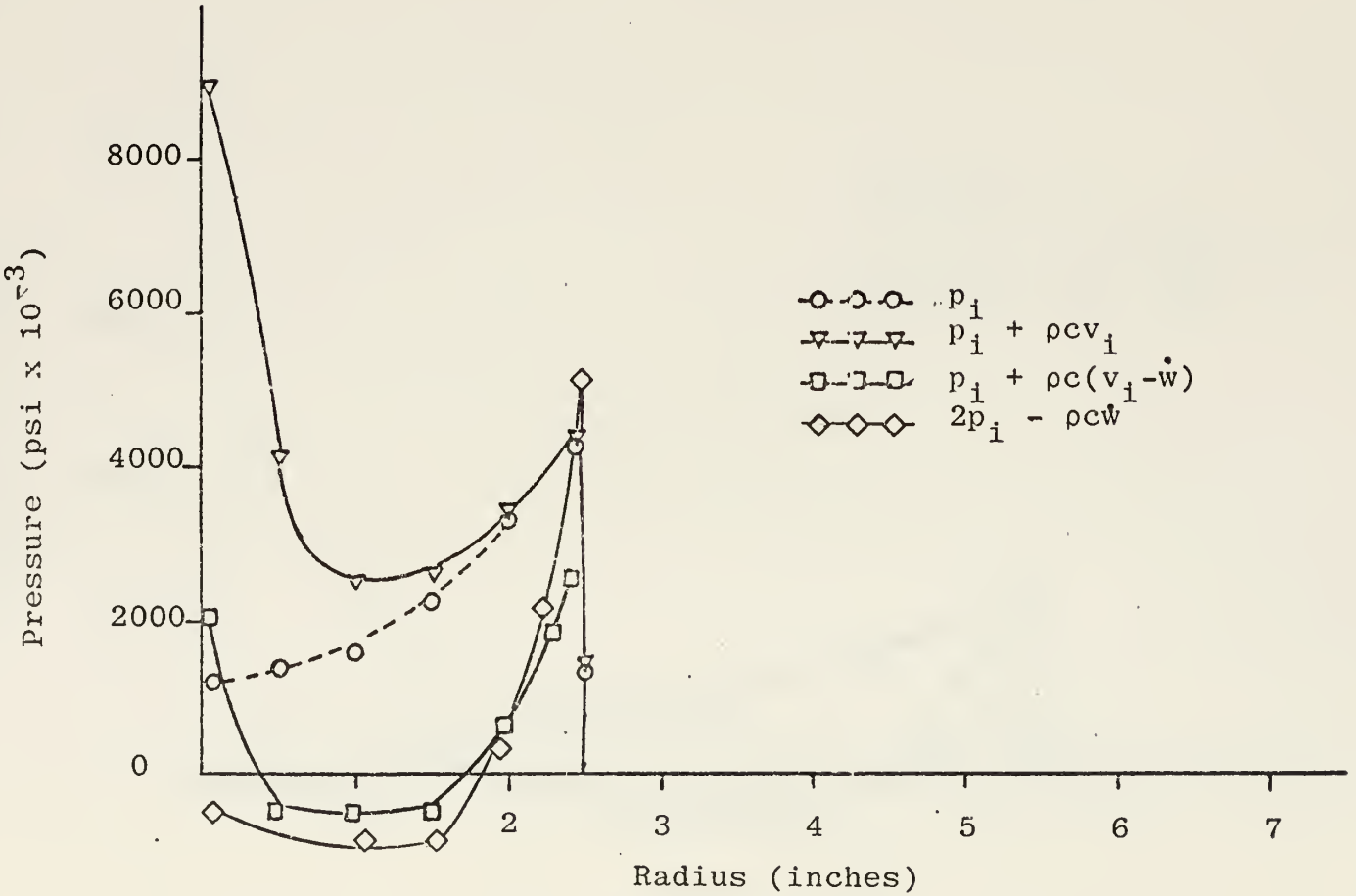

Figure IV-5. Entry Wall Pressure 50 μsec After Impact

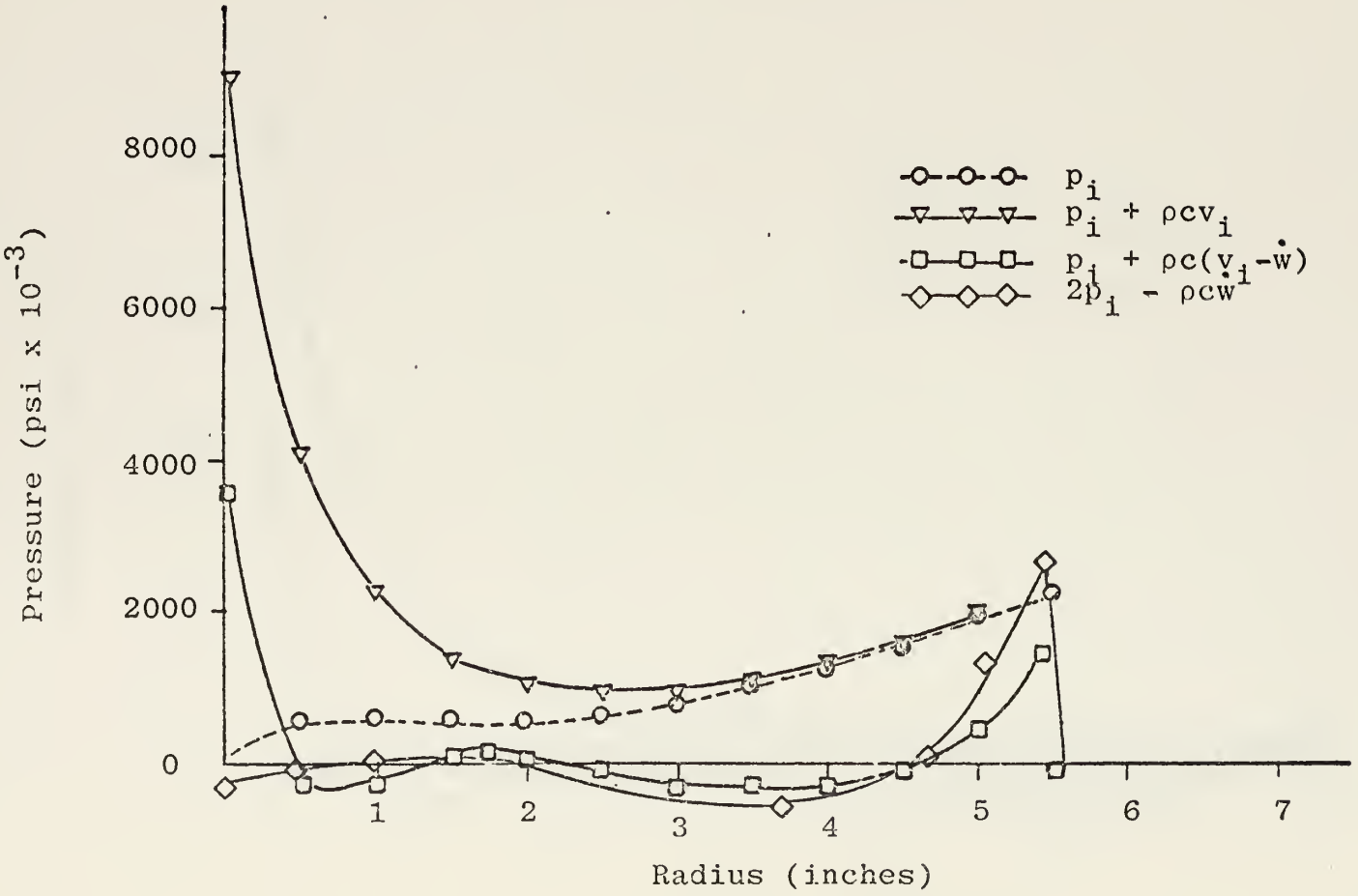

Figure IV-6. Entry Wall Pressure 100 μsec After Impact

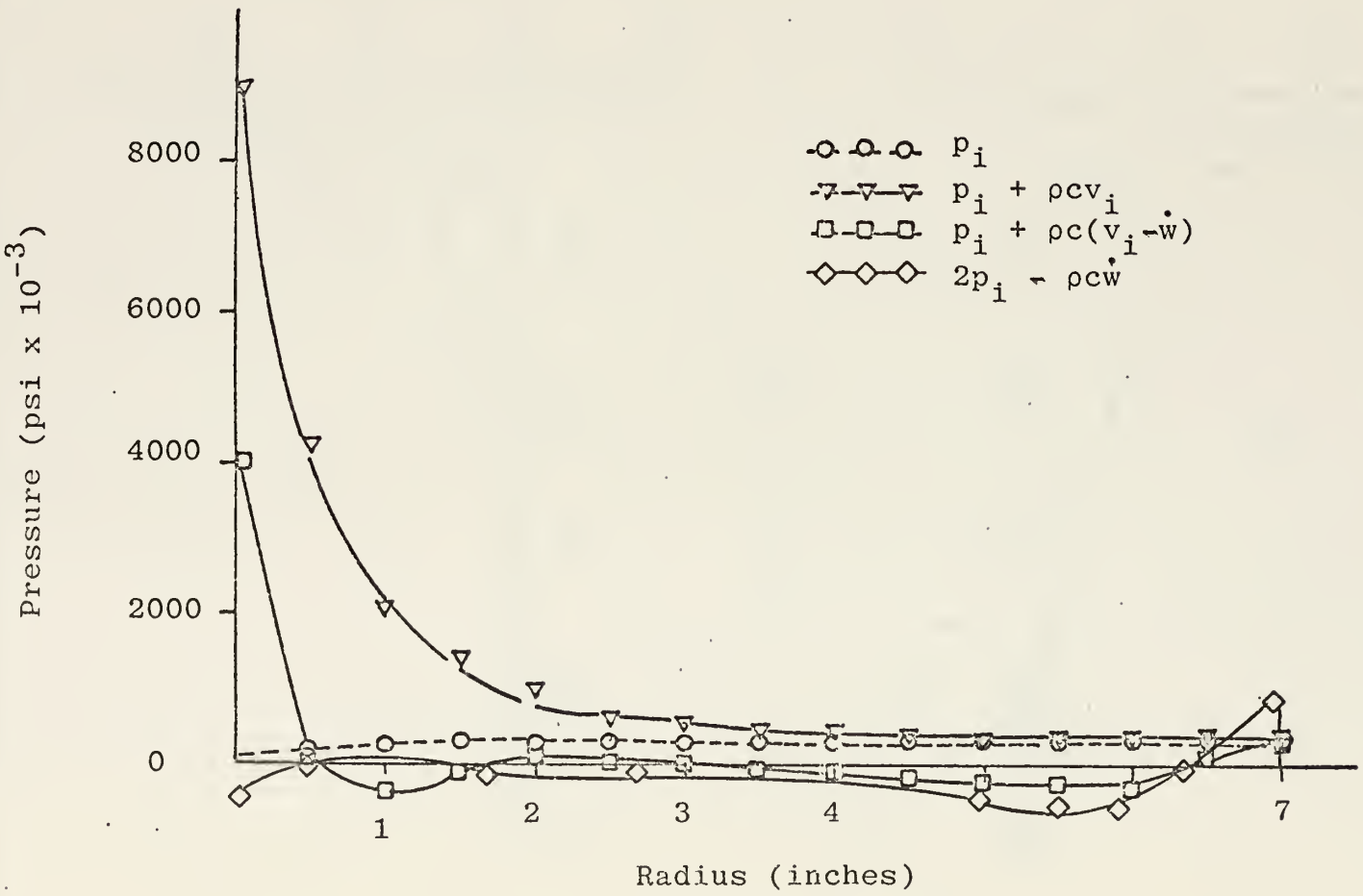

Figure IV-7. Entry Wall Pressure 150 μsec After Impact

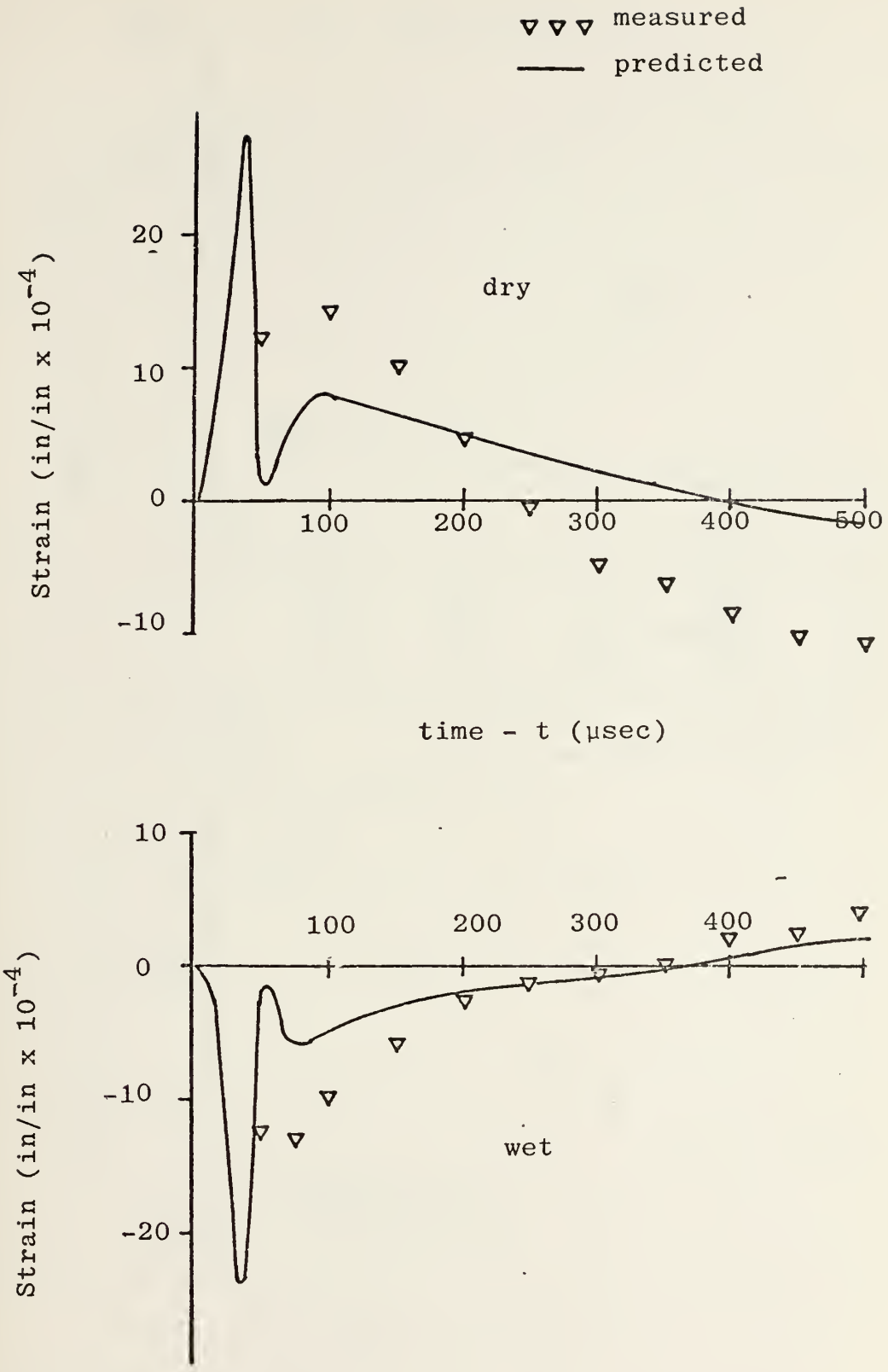

Figure IV-8. Radial Wall Strain With Modified Piston Theory

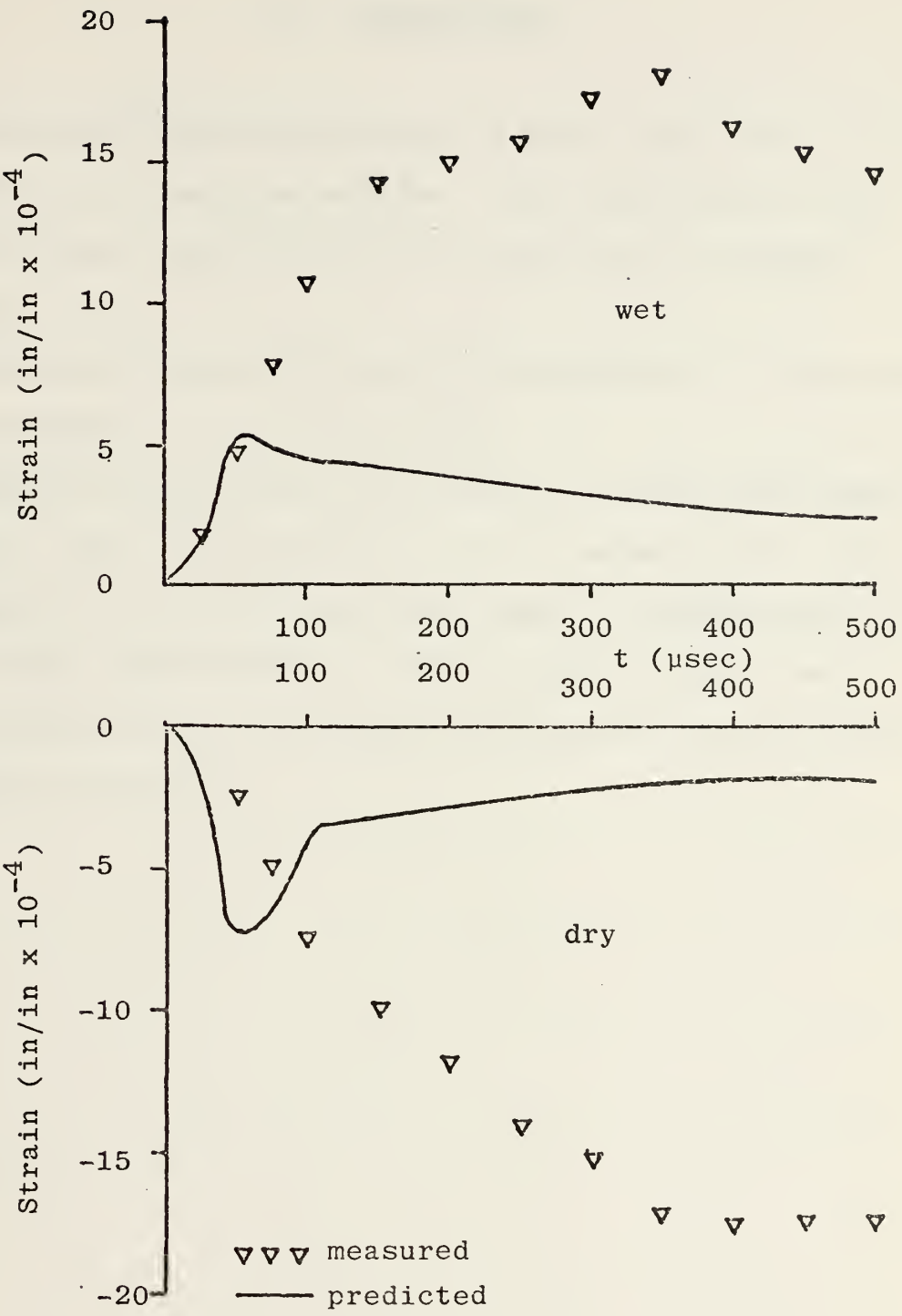

Figure IV-9. Circumferential Wall Strain with Modified Piston Theory

V. CONCLUSIONS

1. The predicted response shows a shock phase that is not evident in the measured strains. This may be due to the fact that the shock front is not sharp but is somewhat smeared.

2. Fluid-wall interaction must be considered if reasonable wall response is to be calculated.

3. The two piston theory load cases bound the experimental results. The full pressure $p_i + \rho c v_i$ causes a very large pressure at the plate center and leads to strains much larger than those measured. The $2p_i$ case leads to an underestimation of the strains, particularly in the circumferential direction.

LIST OF REFERENCES

1. Boeing Company report No. C 162-10294-1, Hydraulic Ram, by R. G. Blaisdell, September 1970.

2. McDonnel Aircraft Engineering Methods Authorization, F65-76-555, Hydraulic Ram: A Fuel Tank Vulnerability Study, by R. N. Yurkovich, September 1969.

3. Naval Weapons Center Technical Publication, 5227, Fluid Dynamic Analysis of Hydraulic Ram, by E. A. Lundstrom, July 1971.

4. Naval Postgraduate School Report 57Bp74071, Aircraft Fuel Tank Vulnerability to Hydraulic Ram: Modification of the Northrop Finite Element Computer Code BR-1 to Include Fluid-Structure Interaction, R. E. Ball, July 1974.

5. NASA Contractor Report, NASA Cr-1987, A Computer Program For The Geometrically Nonlinear Static and Dynamic Analysis of Arbitrarily Loaded Shells of Revolution, Theory and Users Manual, by R. E. Ball, April 1972.

6. C. C. Perry and H. R. Lissner, The Strain Gage Primer, 2nd ed, McGraw-Hill, 1962.

7. Stein, Peter K., Measurement Engineering, Applications, 2nd ed., Stein Engineering Services, Inc., 1962.

8. Naval Weapons Center Report, JTCG/AS-74-T-018, Fluid Dynamic Analysis of Hydraulic Ram IV, by E. A. Lundstrom and W. K. Fung, December, 1974.

9. Power, H. L., FY 74 Experimental Hydraulic Ram Studies, NPS-57Ph74081, August 1974.

10. Holm, C. M., Hydraulic Ram Pressure Measurements, MSAE Thesis, Naval Postgraduate School, Monterey, California, December 1974.

INITIAL DISTRIBUTION LIST

		No. Copies
1.	Defense Documentation Center Cameron Station Alexandria, Virginia 22314	2
2.	Library, Code 0212 Naval Postgraduate School Monterey, California 93940	2
3.	Chairman, Department of Aeronautics, Code 57 Naval Postgraduate School Monterey, California 93940	1
4.	Professor H. L. Power, Jr., Code 57Ph Department of Aeronautics Naval Postgraduate School Monterey, California 93940	6
5.	Professor R. E. Ball, Code 57Ba Department of Aeronautics Naval Postgraduate School Monterey, California 93940	3
6.	Captain James McNerney DDR & E Pentagon Department of Defense Washington, D. C. 20301	1
7.	CDR Merlin L. Johnson Naval Air Systems Command Washington, D.C. 20360	1
8.	CDR D. Hicks Naval Air Systems Command Washington, D.C. 20360	1
9.	Mr. Andy Holton AFDL/PTS Wright Patterson AFB Ohio 45433	1
10.	LCDR Bruce D. Page USS Saratoga, CV-60 FPO New York, N.Y. 09501	2
11.	Mr. Wallace K. Fung, Code 5114 Naval Weapons Center China Lake, California 93555	2